

Article

Extensive Experimental Characterization with Kinetic Data for the Gasification Simulation of Solid Biofuels

Maximilian Robert Heinrich ^{1,*}, André Herrmann ², Andy Gradel ¹, Marco Klemm ² and Tobias Plessing ¹ 

¹ Institute for Water and Energy Management, University of Applied Sciences Hof, 95028 Hof, Germany; andy.gradel@hof-university.de (A.G.); tobias.plessing@hof-university.de (T.P.)

² DBFZ Deutsches Biomasseforschungszentrum Gemeinnützige GmbH, 04347 Leipzig, Germany; andre.herrmann@dbfz.de (A.H.); marco.klemm@dbfz.de (M.K.)

* Correspondence: maximilian.heinrich.2@hof-university.de; Tel.: +49-9281-409-4583

Abstract: In this study, biomass-specific gasification data is experimentally collected for numerical simulations of fixed-bed reactors. Since biomass properties vary, it is crucial to have characteristic biomass data. Extensive data is collected to determine an appropriate description of specific biomass behavior, including basic data (e.g., heating value, size, densities, ultimate and total analysis etc.), biomass pyrolysis and heterogeneous gasification reaction data. Heterogeneous reactions were comparatively investigated in the forms of powder, particles, and a fixed-bed. The powder was investigated in depth with CO₂, O₂, and H₂O (gas fraction 5–20 vol.%; temperature CO₂, O₂ and H₂O, respectively, at 730–790 °C, 360–405 °C, 720–780 °C), while particle reactions and fixed-bed reaction were only studied with CO₂. A model description for a fixed-bed batch reactor was applied, modified, and compared to experimental fixed-bed batch reactor results. This study concludes that determining the appropriate characteristic particle size and parameters for the porous structure of specific biomass char is essential for simulation based on preliminary biomass characterization. Therefore, in future investigations, the description for biomass-specific differences between powder, single particles, and bulk of biomass char may be of greater focus, also taking into consideration O₂ and H₂O.

Keywords: biomass; gasification; pyrolysis; kinetics; downdraft gasifier; spruce; char combustion; boudouard reaction; steam gasification; simulation



Citation: Heinrich, M.R.; Herrmann, A.; Gradel, A.; Klemm, M.; Plessing, T. Extensive Experimental Characterization with Kinetic Data for the Gasification Simulation of Solid Biofuels. *Energies* **2023**, *16*, 2888. <https://doi.org/10.3390/en16062888>

Academic Editor: Grzegorz Czernski

Received: 21 February 2023

Revised: 10 March 2023

Accepted: 14 March 2023

Published: 21 March 2023



Copyright: © 2023 by the authors. Licensee MDPI, Basel, Switzerland. This article is an open access article distributed under the terms and conditions of the Creative Commons Attribution (CC BY) license (<https://creativecommons.org/licenses/by/4.0/>).

1. Introduction

Several scientific and experimental efforts have been made to harvest energy from alternative sources such as solar, water, wind, geothermal and biomass. For the latter, thermal biomass gasification is a widely explored scientific field of research with many facets [1]. Due to the rising demand for renewable energies, there is still the necessity of enhancements and improvements in the field of biomass gasification. It can be primarily divided into the following processes [2–5]:

- drying (evaporation of humidity water);
- pyrolysis (further devolatilizing to char, tar, water, and gas);
- tar cracking (secondary tar reactions);
- homogeneous reactions;
 - water-gas shift reaction;
 - combustion of H₂, CO, gaseous hydrocarbons (e.g., mainly CH₄) and tars;
- heterogeneous reactions;
 - char combustion;
 - Boudouard reaction;
 - steam gasification.

The purpose of this study is to identify suitable biomass-specific characteristics of the previously named processes for modelling syngas production in fixed-bed downdraft gasification. Syngas enables the use of biomass as a source for heat and power generation, as well as a natural gas substitute for industrial process heat and more applications.

Many approaches have been made in the literature to mathematically describe the pyrolysis and gasification of biofuels. Basu et al. [6] classify the modelling into thermodynamic equilibrium, kinetic, computational fluid dynamics (CFD), and artificial neural network (ANN). Further, the benefits of computer models such as finding optimum conditions or assisting up and down scaling with less experimental time and effort are mentioned.

In 2019, a promising approach for a fixed-bed downdraft reactor model with integrated tar adsorption was developed by Gradel et al. The model is based on standardized wood pellets as fuel. The parameters and data used for modelling were obtained by studies (e.g., homogeneous reaction kinetics, pyrolysis data) but also from self-performed measurements (heterogeneous reaction kinetic data, pyrolysis data and BET analysis) [4].

In 2011, Neves et al. made an extensive summary of pyrolysis research in their work, showing that many studies in the field of pyrolysis with a vast variety of biomass were conducted [7]. But this also leads to a lack of comparability when it comes to comparing the process behavior of a specific type of biomass. Although the first table in the work of Neves et al. might not contain every biomass study, only a few types of biomasses can be found more than three times in the reviewed studies. Furthermore, the varying experimental setups used in the research of Neves et al. have resulted in a wide range of results, making it difficult to use them as comparable biomass-specific pyrolysis and gasification data. Beech and pine were the most common found wooden biomass in the research papers investigated by Neves et al. It is important to mention that not every study presented in [7] was additionally evaluated here for beech and pine data.

In 2017, Morin et al. studied the kinetics of biomass char combustion. Their review of the literature lists some research in this field [8]. They also concluded the following dependencies in reactivity based on studies and experiments:

1. An increase in the particle heating rate increases the reactivity of char [9–13];
2. Higher pyrolysis pressure decreases char reactivity [10–14];
3. Residence time at final pyrolysis temperature: either decrease of reactivity [11,15] or no effect [13];
4. Higher final temperature leads to decrease of reactivity [16];
5. Also highly depending on chemical structure and ash content, which refers to the nature of biomass [16].

Therefore, a different type of biomass char has varying reaction characteristics. Morin et al. primarily investigated combustion behavior. The kinetics for char gasification agents like CO₂ and H₂O were mentioned but not in focus [8]. In 2010, Irfan et al. specifically reviewed coal gasification in a CO₂ atmosphere [17]. Yet, the combined characterization with pyrolysis and the gasification agents CO₂, O₂ and H₂O is not commonly reported in the literature. As a result, there is a lack of data available for characterization of one specific biomass for kinetic reactor modelling purposes. Thus, this work aims for an extensive characterization with consideration of elemental analysis, pyrolysis behavior and products, and intrinsic char reactivity with CO₂, H₂O, O₂, considering different scales (intrinsic, particle, bed), to provide more reliable and reproducible biomass-specific data for more accurate mathematical models.

2. Materials and Methods

Spruce in the form of defined wooden chips (DWC) was used as a reference fuel. They were processed by chipping and sufficient sieving to contain a homogeneous size between 12 mm and 16 mm. The defined wooden chips contained nearly no bark. A sample of the chosen biomass is shown in Figure 1. The biomass was primarily chosen in consideration of particle size and size distribution, availability, and a high ratio of domestic spruce logging in Germany (74.8% in 2021) [18]. For ultimate analysis, a Vario Macro Cube from Elementar

Analysensysteme GmbH (Langensfeld, Germany) was used, in the manner of DIN EN ISO 16948 [19].



Figure 1. Sample of the defined wooden chips used in this study. Containing spruce with particle size of 12 to 16 mm and nearly no bark with a ruler for size comparison.

The total analysis procedure was conducted with ICP–OES in accordance with DIN EN ISO 16967;2015-07 [20] and DIN EN ISO 16968;2015-09 [21]. Ash content was measured in the manner of DIN EN 14775 (550 °C) [22] for biomass and DIN 51719 [23] for the pyrolysis char. Water content was determined with DIN EN 14774-2 [24]. Volatile matter was analyzed with DIN EN ISO 18123 [25].

The evaluated properties of the biomass are listed in Table 1. For true density, apparent (particle) density and particle porosity of spruce char, the values evaluated by Dufourny et al. [26] were used. Bulk density was measured by filling a beaker (1000 mL for biomass, 200 mL for char) to a defined volume and measuring the mass five times and again by another person. The calculated bulk density was averaged. The Sauter diameter was calculated as in DIN EN ISO 9276-2 [27].

Table 1. Properties and information of the investigated biomass.

Description and Properties	Values		Unit	Comments
	Wood	Char		
type	spruce	-	-	not further specified
origin	calamity wood germany	-	-	-
particle size	>1 mm	0.1 wt.%	-	DIN EN 15149-1 [28]
	>3.15 mm	1.7 wt.%	-	-
	>8 mm	96.9 wt.%	-	-
	>16 mm	1.3 wt.%	-	-
average dimensions	16 × 11 × 4	11 × 8 × 3	mm	statistical ($n = 30$)
Sauter diameter, $\bar{x}_{1,2}$	0.0105	0.0076	m	DIN EN ISO 9276-2 [27]
bulk density	178.4	118.8	kg m ⁻³	statistical ($n = 10$)
true density	-	1850	kg m ⁻³	[26]
apparent density	405	221	kg m ⁻³	[26]
particle porosity	-	0.88	-	[26]
HHV	20,080	32,500	kJ kg ⁻¹	DIN EN ISO 18125 [29]
LHV	18,790	31,830	kJ kg ⁻¹	DIN EN ISO 18125 [29]
bark fraction	<1	<1	wt.%	-
ash content at 550 °C	0.38	1.5	wt.% (dry)	DIN EN 14775 [22]

Table 1. Cont.

Description and Properties	Values		Unit	Comments
	Wood	Char		
ash content at 855 °C	-	1.55	wt.% (dry)	DIN 51719 [23]
water content	15.2	2.6	wt.%	DIN EN 14774-2 [24]
volatile matter	84.5	-	wt.%	DIN EN ISO 18123 [25]
ultimate analysis				DIN EN ISO 16948 [19]
C	51	85.9	wt.% (dry)	-
H	6.09	2.93	wt.% (dry)	-
S	n.d.	n.d.	wt.% (dry)	not detectable (below detection limit)
O	42.91	10.84	wt.% (dry)	calculated residual
N	n.d.	n.d.	wt.% (dry)	-
ICP-OES Total analysis	24 elements	24 elements	mg kg ⁻¹	DIN EN ISO 16967 [20] DIN EN ISO 16968 [21] results in Appendix A

The results of small-scale experiments (advanced properties and powder gasification) are used to calculate and compare particle and fixed-bed experiments to indicate and precise the main data needed for fixed-bed gasification simulation and improve the model used.

2.1. Fixed-Bed Batch Reactor Wood Chip Pyrolysis

A batch of around 500 g of fuel was pyrolyzed as a fixed-bed in a laboratory-scale reactor to characterize the pyrolysis reaction via mass balance. The reaction products were char inside the reactor, product gas with liquids (respectively, tar and water) and gaseous parts, which were measured. The used fixed-bed batch reactor is located at the DBFZ in Leipzig (Figure 2). The reactor can be described as an inverted downdraft reactor. It is electrically heated at the bottom and sidewalls with adjustable power up to 8.8 kW. Preliminary tests were done to reach a target heating rate of 7–16 K min⁻¹. To ensure the feasibility of experiments, the measurement devices were comparably checked and/or calibrated.

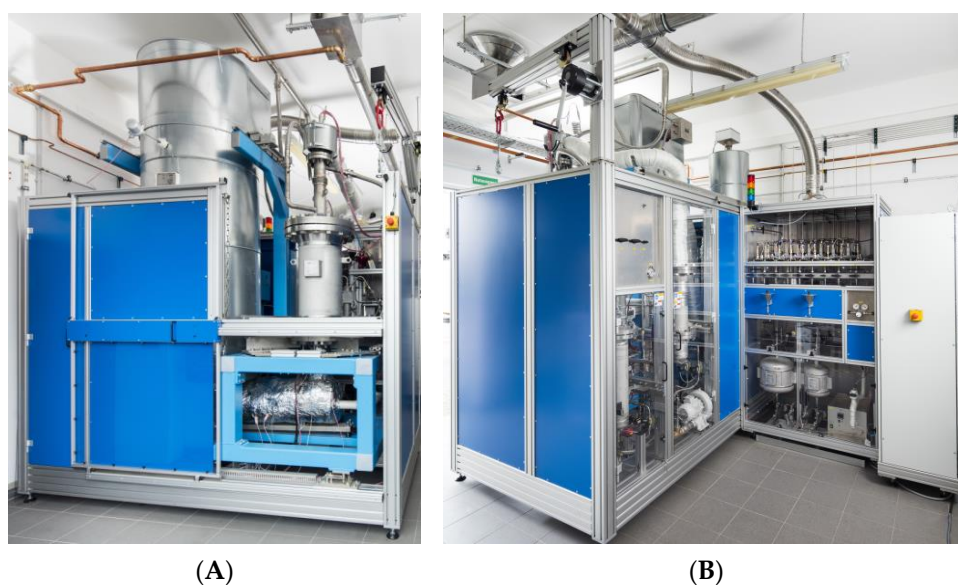


Figure 2. DBFZ fixed-bed batch reactor for characterizing pyrolysis und gasification reaction. (A) Front side with preheater for gasification agent (left) and reactor (right); (B) back side with product gas handling (left) and mixing station for gasification agents (right).

The plant consists of several preheaters and a bypass for heating at the beginning, as well as the reactor and product gas cooling. Inside the reactor are 15 thermocouples to measure the axial and wall temperature profile (Figure 3) during the experiment. Gas analyzers were installed to measure H_2 , CO , CH_4 , CO_2 , O_2 , N_2 , C_2H_6 , and C_2H_4 in the cooled ($5^\circ C$) dry gas. At the beginning and end of the experiments, the gas analyzers were checked with test gas to determine and document the measurement errors. N_2 , O_2 , steam, CO_2 and mixtures thereof were available as feed gas in the range up to 3500 L min^{-1} (STP). The several preheaters heat the reactor feed gas up to $700^\circ C$ in bypass of the cold reactor. After the target temperature had been reached, the hot gas was switched from the bypass to the reactor with a fixed-bed of wood or char. After gasification or pyrolysis inside the reactor, the resulting product gas was transported to the cooler at $450^\circ C$, cooled down to $10\text{--}20^\circ C$ and analyzed with micro gas chromatography (μGC), Fourier-transform infrared spectroscopy (FTIR), optical oxygen sensor and diaphragm gas meters.

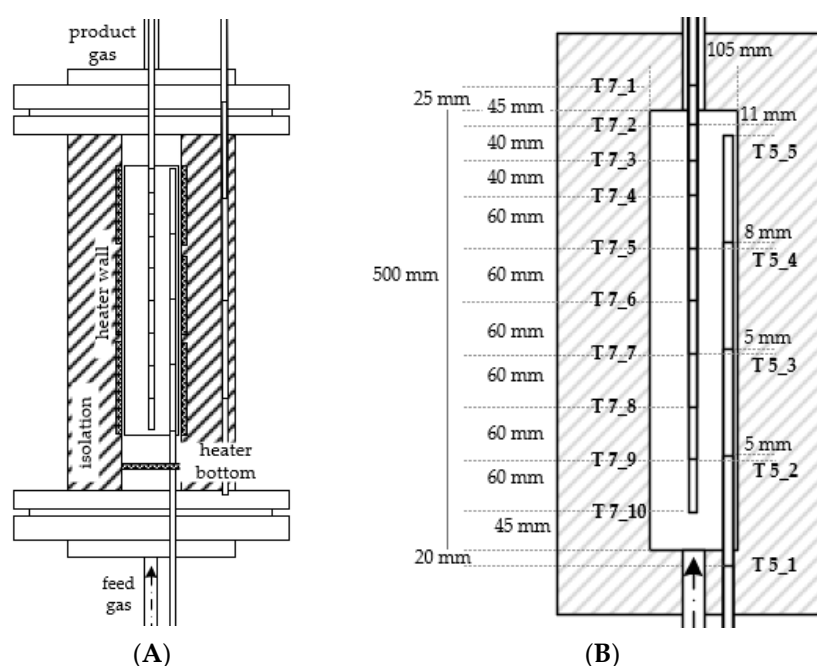


Figure 3. (A) scheme of DBFZ batch reactor with two multipoint thermocouples; (B) scheme of thermocouples positions and names inside the reactor.

The target temperature for the first pyrolysis experiments was $500^\circ C$. Preliminary tests showed that the reactor temperature varied over the complete height by $50\text{--}100^\circ C$. This is due to the reactor geometry and massive connectors dissipating heat close to the upper and lower ends of the heating zone while warming up. To ensure a minimum pyrolysis temperature of $450^\circ C$, the target process temperature was set to $500^\circ C$ to prevent heterogeneous reactions between char and CO_2/H_2O . The process was continuously purged with preheated nitrogen at $500^\circ C$ (Figure 4). The measured heating rate was $7\text{--}10\text{ K min}^{-1}$. The heating rate was chosen in that range, so that the pyrolysis speed was nearly comparable with the planned use of a real gasification plant later in the project. Gas composition was also tracked during this process. A fine-meshed steel basket (1.4841/AISI 314) holds during pyrolysis with a diameter of 100 mm and a filling height of around 500 mm . The vertical temperature profile was measured in the center of the bed every 60 mm (Figure 3) and horizontal at the outer rim of the bed at a height of 120 mm to further monitor local temperatures. After reaching the target temperature, the process was continued until no more product gases were detected (i.e., about 90 min). The product gas was cooled down to $10\text{--}20^\circ C$ to collect condensable parts in a trap system.

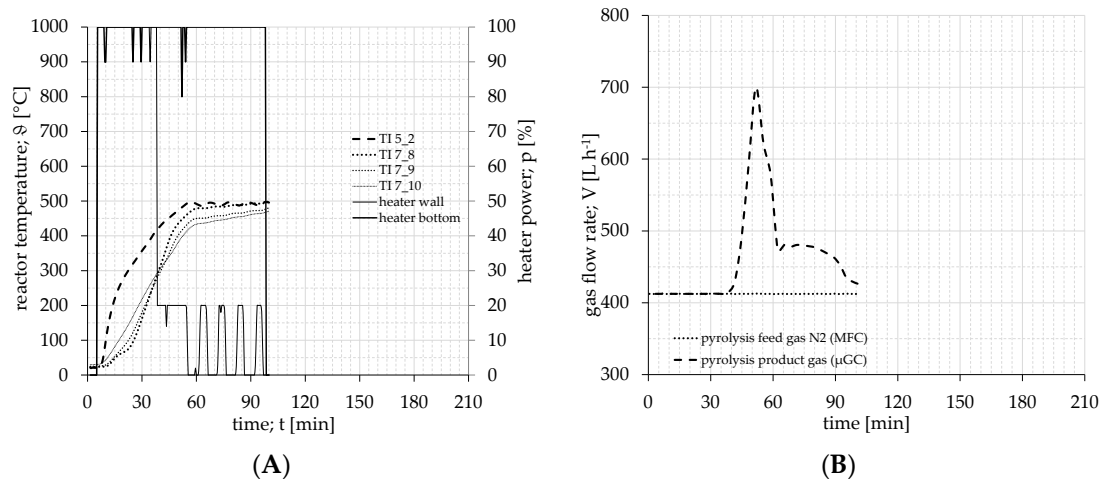


Figure 4. Pyrolysis (2021-00084) of wood chips in one step with 500 °C: (A) temperature profile; (B) profile of pyrolysis feed gas and product gas.

Afterwards, the char was weighed and summed up with the fuel-input and gas-output (calculated from the gas components and inert nitrogen flow) for the mass balance. The difference between input (fuel) and output (gas, char) is the condensable parts (water and tar).

After characterization, the pyrolysis at 500 °C and pyrolysis at 850 °C were started. The experimental procedure was identical to the pyrolysis with 500 °C up to the reactor temperature. The target of the 850 °C-pyrolysis was the characterization of the pyrolysis reactions and preparation of pyrolysis char for further use for CO₂ gasification experiments. If the pyrolysis coke is prepared at 500 °C and then heated to 800 °C, for the subsequent gasification reaction, pyrolysis resumes above 500 °C, which then superposes the gasification reaction; therefore, the pyrolysis temperature was raised to 850 °C. Figure 5A shows the temperature profile inside the fuel/char fixed-bed and flow of nitrogen (Figure 5B). As with the 500 °C pyrolysis, the experiment with 850 °C was stopped only when no pyrolysis gas was measured in the reactor product gas (Figure 5B). After pyrolysis, the char was taken out of the reactor for weighing and refilled into the reactor for gasification.

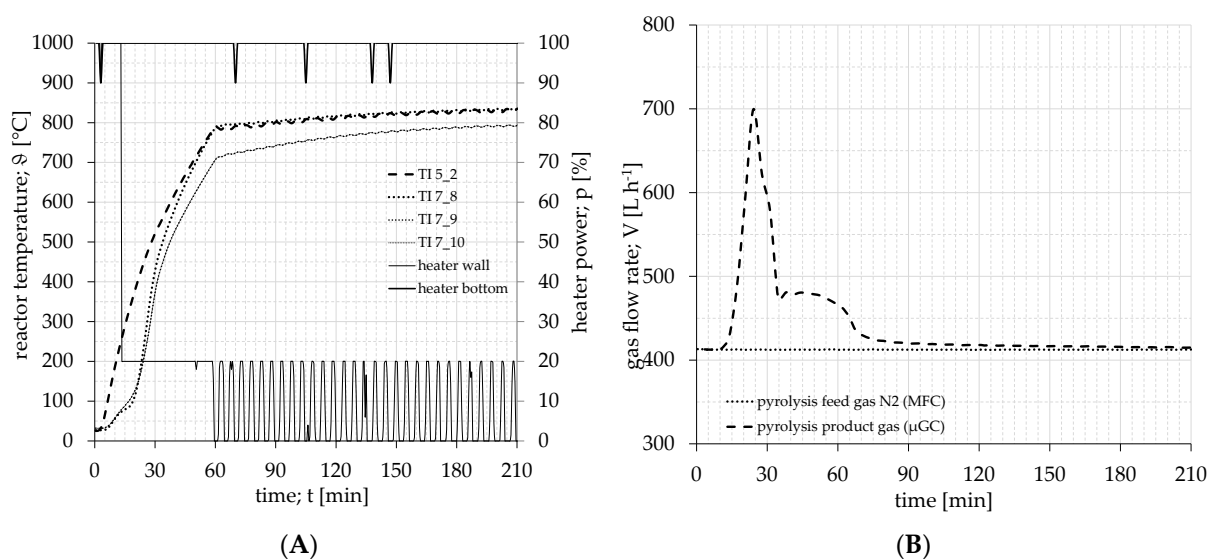


Figure 5. Pyrolysis (2022-00041) of wood chips in one step with 850 °C: (A) temperature profile; (B) profile of pyrolysis feed gas and product gas.

However, subsequent CO₂ gasification reactions with 850 °C char showed that the pyrolysis temperature is furthermore too low to accurately characterize the char-gasification reaction at 850 °C. Since the fixed-bed does not reach 850 °C everywhere during 850 °C pyrolysis, it was found in initial tests that few pyrolysis reactions still proceed. Thus, the pyrolysis temperature was raised from 850 °C to 900 °C (Figure 6) to be able to simultaneously exclude occurring pyrolysis reactions during the subsequent CO₂ gasification. The measured heating rate for these experiments was 12–13 K min⁻¹ similar to pyrolysis at 500 °C with 7–10 K min⁻¹.

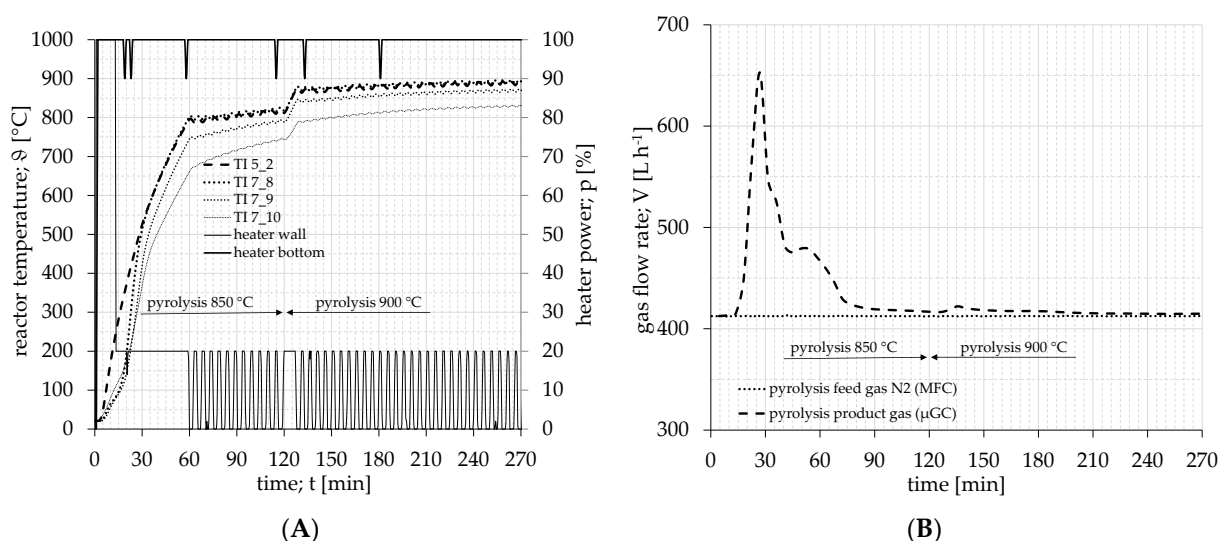


Figure 6. Pyrolysis (2022-00057) of wood chips in two steps with 850 °C and 900 °C: (A) temperature profile; (B) profile of pyrolysis feed gas and product gas.

The temperature profile and gas flow were identical to those of the previous 850 °C tests until the temperature was changed to 900 °C. After the temperature was changed to 900 °C, the temperature in the fixed-bed was increased in conjunction with an increased outgassing of the fuel. This shows a peak in the product gas ratio after 120 min. Here, too, the experiment was only stopped when no more pyrolysis gas could be measured in the product gas of the reactor.

2.2. Char Powder Gasification

The thermogravimetric analysis (TGA) was performed on an STA 449 F5 Jupiter (manufacturer: NETZSCH-Gerätebau GmbH, Selb, Germany) under atmospheric pressure with nitrogen as the protective purge gas. The reactive gases were CO₂, O₂ and H₂O. To determine the intrinsic rate of reaction in a TGA, some pieces of the produced pyrolysis char were ground down with a small laboratory mortar and pestle. The char powder was sieved through a 25 µm stainless steel mesh. Thus, a particle size smaller than 62 µm can be obtained for measurements as mentioned by Magnaterra et al. [30]. The powder showed a specific surface area of dimension 350 m² g⁻¹ in a BET-Measurement.

Figure 7 shows images from a scanning electron microscope (SEM; type: JEOL JSM-6360) for structure and size investigation. Comparing the leftover powder particles from sieving (Figure 7A) and the sieving product powder (Figure 7B), the wooden structure was abolished and the small particle size was achieved.

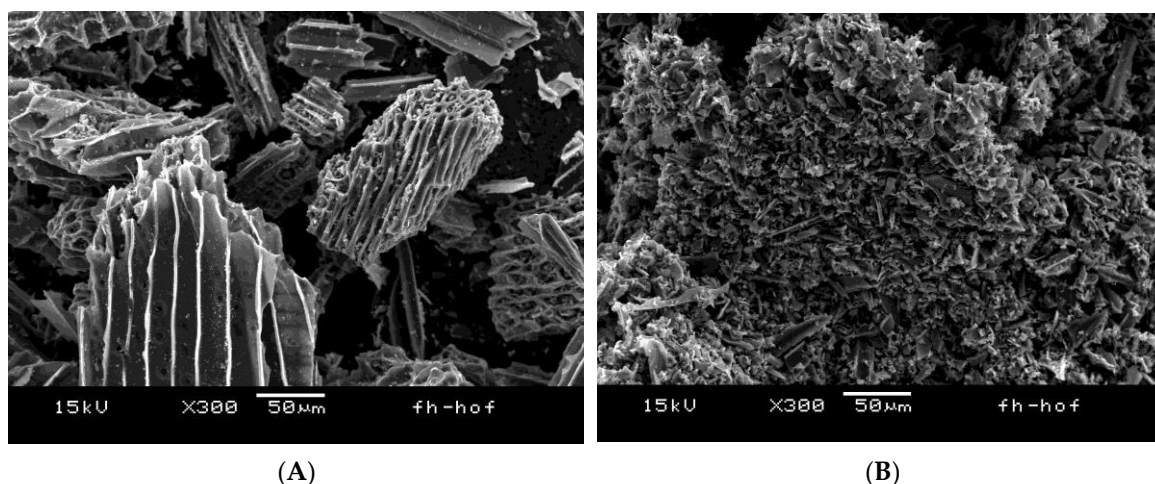


Figure 7. Scanning electron microscope images of the used biomass charcoal for size and structure investigation: (A) leftover particles from sieving; (B) sieving product powder.

The samples were measured in a cylindrical 85 μL aluminum oxide crucible (inner diameter 5.9 mm and inner height 3.7 mm). The crucibles were placed on a differential scanning calorimetry (DSC) sample carrier to make use of an automatic sample changer (ASC).

The sample weight of all samples was $2 \text{ mg} \pm 0.2 \text{ mg}$. Special care was taken to spread the powder uniformly on the bottom of the crucible to provide a very thin layer and further minimize diffusion effects, as also mentioned by Magnaterra et al. [30].

The total gas flow rate was set to 200 mL min^{-1} during measurement. With an inner diameter of 26 mm and a temperature of $800 \text{ }^\circ\text{C}$, the estimated gas velocity was 20 mm s^{-1} . Passing the round DSC sample carrier with a diameter of 23.5 mm, the gas may be accelerated to 105 mm s^{-1} . At a low reactive volume fraction of 5%, the gas flow may replenish reactive gas for a reaction of 0.09 mg s^{-1} , which is 13 times the maximum rate measured at $950 \text{ }^\circ\text{C}$ and $v_{f,\text{CO}_2} = 20 \text{ vol.}\%$. Thus, the feed of reactive gas is considered to continuously provide the target gas concentration at the top of crucible throughout the experiments.

The reactive gas was set with the internal mass flow controller (MFC) to the gas concentrations, respectively (e.g., $160 \text{ mL min}^{-1} \text{ I}_2$ with $40 \text{ mL min}^{-1} \text{ CO}_2$ for $v_{f,\text{CO}_2} = 20 \text{ vol.}\%$). The purity of gases were 99.999% for N_2 and O_2 and 99.995% for CO_2 . The temperature program of a measurement was set up as described in Table 2.

Table 2. STA steps for measurement of heterogeneous reaction rates.

Step	Mode	Temperature [$^\circ\text{C}$]	Heating Rate [K min^{-1}]	Duration [min]	Gas Flowrate [mL min^{-1}]	Comments
#1	start	40	-	-	200 N_2	-
#2	heating 1	to 130	20	-	200 N_2	-
#3	isothermal	at 130	-	30	200 N_2	to fully evaporate the humidity and inertization
#4	heating 2	$T_{\text{target}} - 15$	20	-	200 N_2	fast heating to approximate T_{target}
#5	heating 3	T_{target}	5	3	200 N_2	slow heating to acquire T_{target}
#6	isothermal	T_{target}	-	40	200 N_2	time to stabilize after heating
#7	isothermal	T_{target}	-	300	switch to reactive gas mixture with total flowrate of 200	heterogeneous reaction
#8	end	-	-	-	-	-

For H₂O reaction, the process humidity is provided by a modular humidity generator (proUmid MHG32; MHG). Therefore, the humid nitrogen flow of the MHG is added as purge gas and mixed with the protective gas before reaching the sample. The humidity can be controlled by setting the temperature and relative humidity of the MGH-flow.

The MHG-flow was set to a total of 166 mL min⁻¹ and protective gas flow to 34 mL min⁻¹. An adjusted relative humidity of 51.4% at 80 °C leads to a volume fraction of 24.2 vol.% H₂O in MHG-flow. With the 34 mL min⁻¹ protective flow, a volume fraction of 20 vol.% H₂O at a total flow of 200 mL min⁻¹ can be obtained. For lower total volume fractions of 12.5 vol.% and 5 vol.% H₂O, the relative humidity was set to 32.1% and 12.9%, respectively. Fully demineralized water was used. The possible content of O₂ solved in liquid salt-free water is at a maximum of 9.1 mg dm⁻³ at 20 °C [31]. At a volume fraction of 20 vol.% H₂O as reactive gas, the O₂ content is approximately 1 ppm and thus considered negligible.

Preliminary tests were conducted to ensure that nitrogen neutralization is acquired during steps #1 to #3 by N₂ purging with success. After heating in step #4 and #5, isothermal step #6 was performed to stabilize the system. At step #7, the gas flow was changed to the desired volume fraction of reactive gas. After about 60 s, the gas mixture reached the sample.

To find the designated target temperatures T_{target} , a test run with each reactive gas was preliminary made. The sample was heated with the same temperature program as shown in Table 2 with a difference in step #7. Instead of the isothermal step, a heating rate of 0.5 K min⁻¹ was set at a starting temperature of 700 °C, 280 °C and 680 °C for CO₂, O₂ and H₂O, respectively.

The temperature test measurement was conducted with a reactive gas atmosphere of 20 vol.%. Figure 8 shows the mass fraction F_j and rate of conversion with the three reactive gases. Comparing Figure 8A,B, an exponential behavior merely due to the change in temperature is assumed between 720 °C and 800 °C. Similarity is observed to Figure 8C–F only with different temperatures. Thus, T_{target} was determined as listed in Table 3 for the long-term experiments to observe solely isothermal behavior.

Table 3. List of parameters for long-term char powder experiments.

Gas		V01	V02	V03	V04	V05	V06	V07	V08
CO ₂	$T_{\text{target,CO}_2}$ [°C]	770	770	730	750	770	790	770	770
	v_{f,CO_2} [vol.%]	20	20	20	20	20	20	12.5	5
O ₂	$T_{\text{target,O}_2}$ [°C]	390	390	360	375	390	405	390	390
	v_{f,O_2} [vol.%]	20	20	20	20	20	20	12.5	5
H ₂ O	$T_{\text{target,H}_2\text{O}}$ [°C]	760	760	720	740	760	780	760	760
	$v_{f,\text{H}_2\text{O}}$ [vol.%]	20	20	20	20	20	20	12.5	5

2.3. Single Particle Char Gasification

To compare the supposed chemically controlled reaction with a diffusion limited particle reaction, the single particle reactions were investigated. Therefore, a TGA sample carrier with a platinum mesh (100 Mesh/149 µm) was used to enable almost free gas flow at the particle surface. Both the DSC and TGA sample carrier are shown in Figure 9. Particles were placed aside from the thermocouple to eliminate the possibility of an over regulation of temperature due to endothermic reaction close to the thermocouple.

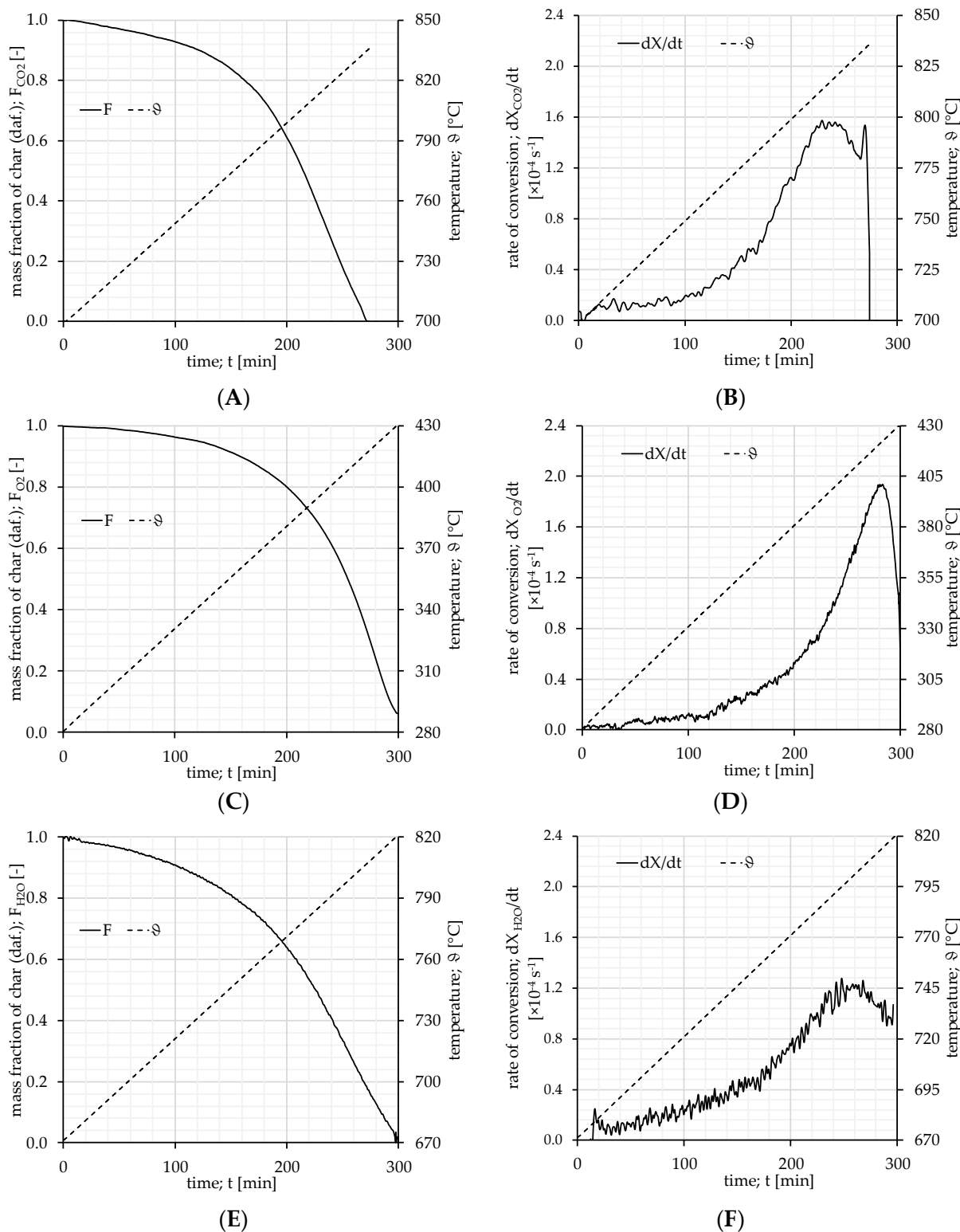


Figure 8. Results from preliminary test to determine T_{target} for long-term experiments with a volume fraction of 20 vol.%. (A) mass fraction from CO₂ Test; (B) rate of mass fraction loss CO₂ Test; (C) mass fraction from O₂ Test; (D) rate of mass fraction loss O₂ Test; (E) mass fraction from H₂O Test; (F) rate of mass fraction loss H₂O Test.

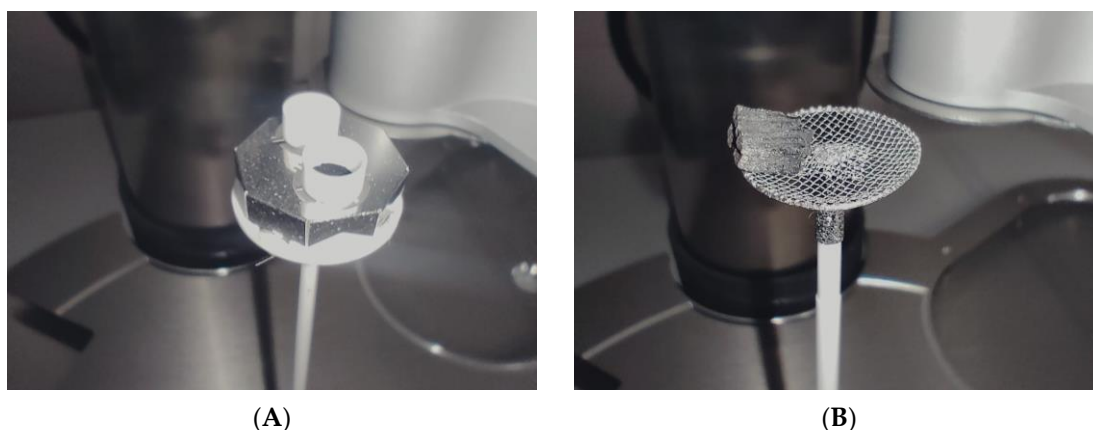


Figure 9. (A) DSC sample carrier with crucible and char powder; (B) TGA sample carrier with a char particle.

The gas flow rate was set to a total of 248 mL min^{-1} . The volume fraction was set to $v_{f,\text{CO}_2} = 0.14$, for comparison with the experiments at the DBFZ's laboratory reactor. Thus, a flowrate of CO_2 was set to 35 mL min^{-1} . Considering a particle with a starting mass of 30 mg , the CO_2 supply by gas flow at $900 \text{ }^\circ\text{C}$ was about six times the estimated chemical reaction rate. The temperature program is equivalent to Table 2. Particle mass was determined on a laboratory scale with $\pm 0.1 \text{ mg}$. The approximated particle size was manually measured with a caliper. To maintain the natural shape and structure, the particles were not sanded to a cuboid form. The temperature was set to $770 \text{ }^\circ\text{C}$, $800 \text{ }^\circ\text{C}$, $850 \text{ }^\circ\text{C}$ and $900 \text{ }^\circ\text{C}$.

Experiments with $850 \text{ }^\circ\text{C}$ were conducted separately and with $v_{f,\text{CO}_2} = 0.125$ to primarily produce different active carbon particles. Yet, the results were averaged and compared due to a small experimental difference of $\Delta v_{f,\text{CO}_2} = 0.015$ compared to the fluctuating reaction rate observed, as later shown in the results.

The reaction rates evaluated from particle measurements were the average rate of the first 25% to 30% of conversion. The mass fraction was calculated as dry ash free (daf). Full decomposition of char was not achieved throughout the experimental time. Thus, the average ash content was used.

2.4. Fixed-Bed Batch Char Gasification

In addition to the gasification experiments at the TGA, the CO_2 gasification was also investigated in the DBFZ fixed-bed batch reactor (Section 2.1). In these experiments, the char of the previous pyrolysis experiments was filled into the batch reactor (nearly 100 g). The char fixed-bed was brought to the target temperature of $800 \text{ }^\circ\text{C}$ with nitrogen directly in the reactor without prior switching to the bypass. After this temperature or a steady temperature profile within the reactor had been reached, CO_2 was switched over as gasification agent. The nitrogen at 1000 L min^{-1} was replaced by a mixture of 905 L min^{-1} nitrogen and 95 L min^{-1} CO_2 (Figure 10). This mixture ratio of nitrogen and CO_2 was determined in coordination with the STA experiments to generate comparable results. Analogously to the pyrolysis experiments carried out before, the product gas concentration and amount were measured after the gas cooling. After 90 min CO_2 gasification, the reactor was cooled with nitrogen (1000 L min^{-1}) and switched-off heaters.

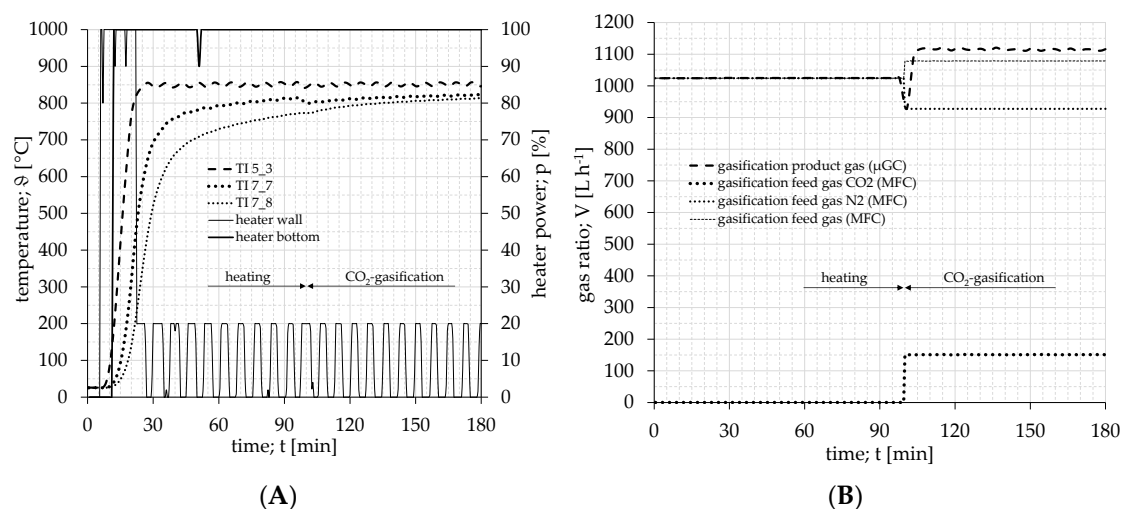


Figure 10. CO₂ gasification (2022-00058) of pyrolysis char (2022-00057): (A) temperature profile; (B) profile of gasification feed gas and product gas.

2.5. Model for Laboratory Reactor

For modelling the laboratory reactor, the adapted equations in Table 4 are used for the special case of the laboratory reactor. Here, a one-dimensional model is used. Therefore, the original with references are given and comparably listed with the adapted equations. The target is to determine more biomass-specific differences between chemical reaction, single particles, and char in a bulk.

It is important to mention that γ is the density of a species per 1 m³ of reactor volume (kg m⁻³_R). The transport of solids and change of solid mass were reduced to a change of mass due to a batch experiment. Diffusive effects were neglected in gas transport between numerical elements. The gas velocity $u_{g,n,i+1}$ for each next timestep regards produced gas and temperature. For the special case of the laboratory reactor, a constant temperature was preliminary assumed and, therefore, energy terms and wall heating equations reduced to given temperatures.

Yet, the temperature could not be held constant over time and height throughout the experiments. Further information can be found in Section 3.4. Thus, the experimental temperature data from laboratory CO₂ gasification was adaptively used to create representative time dependent polynomials (5) and (6) for the two thermocouples T7_7 and T7_8, respectively. Those were interpolated by polynomials of order four and two for T7_7 and T7_8, respectively, with the method of least squares. The subscripts for T7_7 and T7_8 are TC2 and TC1, respectively. For the individual time step, a linear regression between T7_7 and T7_8 was used to estimate the height dependent temperature.

The porosity of the particle was assumed to directly change with the mass of char. Hence, the char reaction rate was used to calculate increasing particle porosity by linking it with the factor $(1 - \varepsilon_{p,0})$.

Drying and pyrolysis were not applied. An effective reaction rate was described by an outer mass transport at the particle surface and effectiveness factor for internal pore diffusion effects, as used for catalysts by Jess and Wasserscheid [32]. Additionally, a modified Thiele–modulus is used with the assumption of a cylindrical particle and correction factor $\omega_{cf,r}$, which is described in Section 3.4 and discussed in Section 4. The binary diffusion coefficient was used with N₂ as secondary gas.

The calculation was performed with MATLAB R2020a and the solver “ode113” was used. The code is provided in the Supplementary Materials.

Table 4. Model equations used to describe the laboratory reactor (equations no. refer to original and adaption left and right side respectively).

Description	Original	Ref.	Adaption for Laboratory Reactor	Equation No.
transport of solids and change of solid mass	$\frac{\partial \gamma_i}{\partial t} = -u_s \frac{\partial \gamma_i}{\partial z} + M_i \sum r_i$	[4]	$\frac{\partial \gamma_{char}}{\partial t} = r_{char} M_{char}$	(1a) (1b)
gas transport and	$\frac{\partial \gamma_j}{\partial t} = -\frac{\partial(u_g \gamma_j)}{\partial z} + \frac{\partial}{\partial z} \left(D_j \frac{\partial \gamma_j}{\partial z} \right) + \epsilon M_j \sum r_j$	[4]	$\frac{\partial \gamma_j}{\partial t} = -\frac{\partial(u_g \gamma_j)}{\partial z} + M_j \sum_j r_j$	(2a) (2b)
gas velocity	not explicitly described in reference		$u_{g,n,i+1} = \left(u_{g,n-1} + \frac{R}{p_0} \frac{n_z}{\epsilon_s} \sum_j \gamma_j \right) \frac{T_{gi}}{T_{gn}}$	(-), (3)
energy and heat transport	$\gamma_s \frac{\partial(T_s c_{p,s})}{\partial t} = -\gamma_s u_s \frac{\partial(T_s c_{p,s})}{\partial z} + \frac{\partial}{\partial z} \left(\lambda_s \frac{\partial T_s}{\partial z} \right) + \sum_n r_n \Delta H_{n,i} + \dot{Q}_{ws} + \dot{Q}_{gs}$	[4]	$T_{TC1}(t) = A_{TC1} t^4 + B_{TC1} t^3 - C_{TC1} t^2 + D_{TC1} t + E_{TC1}$	(5)
	$\gamma_g \frac{\partial(T_g c_{p,g})}{\partial t} = -\gamma_g \frac{\partial(u_g T_g c_{p,g})}{\partial z} + \frac{\partial}{\partial z} \left(\lambda_g \frac{\partial T_g}{\partial z} \right) + \epsilon \sum_m r_m \Delta H_{m,j} + \dot{Q}_{wg} + \dot{Q}_{sg}$		$T_{TC2}(t) = A_{TC2} t^2 + B_{TC2} t + C_{TC2}$	(4), (6)
			$T(z, t) = \frac{T_{TC2} - T_{TC1}}{Z_{TC2} - Z_{TC1}} (z - z_{TC1}) + T_{TC1}$	(7)
			$A_{TC1} = -2.0448 \times 10^{-14}$ $B_{TC1} = 5.5397 \times 10^{-10}$ $C_{TC1} = -4.9341 \times 10^{-6}$ $D_{TC1} = 2.2135 \times 10^{-2}$ $E_{TC1} = 7.6942 \times 10^2$ $A_{TC2} = -6.1077 \times 10^{-7}$ $B_{TC2} = 7.1354 \times 10^{-3}$ $C_{TC2} = 8.0184 \times 10^2$	(8), (-)
wall heater	$\frac{\partial T_w}{\partial t} = \frac{\frac{\partial}{\partial z} (\lambda_w \frac{\partial T_w}{\partial z}) + \dot{Q}_{cl} \frac{d_z}{R} + (\dot{Q}_{gw} + \dot{Q}_{sw}) \cdot dV}{\frac{\pi}{4} (d_{R,o} - d_{R,i})^2 \rho_w c_{p,w} dz}$	[4]	not applied	(9), (-)
particle porosity	$\frac{\partial \epsilon_p}{\partial t} = -u_s \frac{\partial \epsilon_p}{\partial z} - \sum_i \frac{\partial \gamma_i}{(1-\epsilon) \rho_i}$	[4]	$\frac{\partial \epsilon_p}{\partial t} = -r_{char} M_{char} \frac{1}{\gamma_{char,0}} (1 - \epsilon_{p,0})$	(10a), (10b)
water evaporation	$r_v = -S_{p,o} \beta_{H_2O} (c_{H_2O,sat} - c_{H_2O})$	[33]	not applied	(11), (-)
pyrolysis	$r_{pyr} = \frac{-m_{bm} k_{0,pyr}}{M_{bm}} e^{-\frac{E_{A,pyr}}{R \cdot T}}$	[4]	not applied	(12), (-)
mass transport coefficient	$\beta_j = \frac{Sh_j D_{j,N_2}}{d_p}$	[32]	applied	(13), (-)
Sherwood-number	$Sh_j = 1.9 \cdot \left(2 + 0.644 Re^{0.5} Sc_j^{0.33} \right)$	[32]	applied	(14), (-)
binary diffusion coefficient	$D_{j,N_2} = \frac{1.43 \times 10^{-7} T^{1.75} \left[\frac{1}{M_j} + \frac{1}{M_{N_2}} \right]^{\frac{1}{2}}}{\sqrt{2} \left[(G_j)^{\frac{1}{3}} + (G_{N_2})^{\frac{1}{3}} \right]^2}$	[34]	applied	(15), (-)
effective diffusion coefficient	$D_{j,eff} = \frac{\epsilon_p}{\tau} D_{pore}$ with $\tau = 3$ and $D_{pore} = D_{j,N_2}$	[32]	applied	(16), (-)
modified Thiele-modulus	$\Phi = \frac{d_p}{6} \sqrt{\left(\frac{v_{c,j} + 1}{2} \right) \frac{k_{char,j,chem} \rho_c (1 - \epsilon_p) c_j^{v_{c,j} - 1}}{D_{j,eff}}}$	[32]	$\Phi = \omega_{cf} \frac{d_p}{6} \sqrt{\left(\frac{v_{char,j} + 1}{2} \right) \frac{k_{char,j,chem} \rho_{char} (1 - \epsilon_p) c_i^{v_{c,j} - 1}}{D_{j,eff}}}$	(17a), (17b)
effectiveness factor	$\eta = \frac{\tanh(\Phi)}{\Phi}$	[32]	applied	(18), (-)
effective reaction rate	$k_{char,j,eff} = \frac{1}{\frac{1}{S_{p,o} \beta_j c_j^{1-v_{c,j}}} + \frac{1}{\eta k_{char,j,chem}}}$	[35]	applied	(19), (-)

3. Results and Discussion

3.1. Pyrolysis

As result of the different pyrolysis experiments, the measured product gas concentrations are shown in Figure 11. For all three pyrolysis temperatures, the characteristic product gas profile is nearly identical. The profiles are only time-shifted.

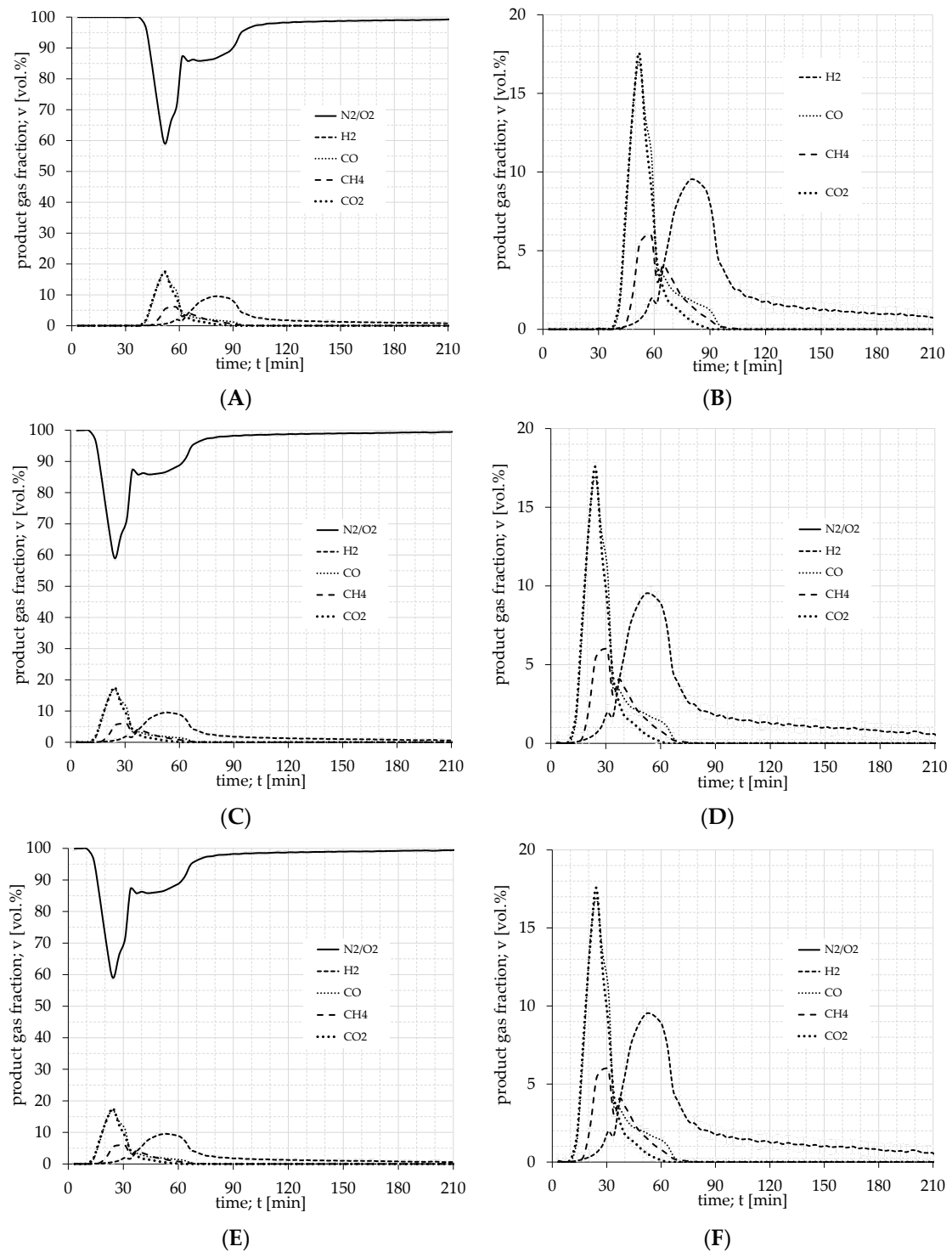


Figure 11. Product gas concentration of pyrolysis of wood chips: (A,B) 500 °C (2021-00084); (C,D) 850 °C (2021-00041); (E,F) 850 °C/900 °C (2021-00057).

First, CO and CO₂ concentrations rise to a peak of 17.5 vol.%. Nearly four minutes later, the CH₄ concentration also rises to a 6 vol.% peak. The CO and CO₂ concentrations decrease uniformly again to 0 vol.%. The CH₄ concentration drops to 3 vol.% and then rises again to a second peak with 4 vol.%. Then, it drops evenly to 0 vol.%. The H₂ concentration rises approximately at the same time as the CH₄-concentration, but with a much flatter increase, resulting in a 9.5 vol.% peak, which takes 35 min to increase. After that, the H₂ concentration drops only as fast as it has risen and then flattens off. At the end of the experiment, the H₂ concentration drops from 1.8 vol.% to 0.6 vol.% in 120 min.

For the pyrolysis experiments at 500 °C, 850 °C and 850 °C/900 °C for several measurements, the following mass balances could be established. They show a stable ratio between the product components (char, gas, condensate in relation to the fuel-input) for the different experiments. So, the input-fuel was transformed by pyrolysis: 500 °C to 25–26% char, 14–15% dry gas and 59–61% condensable parts (water and tar). By pyrolysis with 850 °C and 850 °C/900°C, the fuel transformed to 21–22% char, 18–19% dry gas, and 57–61% condensable parts. An overview is provided in Table 5. The condensable components are calculated as the difference between input (fuel) and output (char and gas) and cannot be detected or separated by measurement technology with the currently existing experimental setup. In the future, the condensable components are to be separated by measurement using a steam analyzer or FTIR in the hot product gas. The composition of dry gas is shown in Table 6.

Table 5. Pyrolysis products at different temperatures and a heating rate of 7–10 K min⁻¹.

Experiment Number	Pyrolysis Temperature [°C]	Heating Ratio [K min ⁻¹]	Input			Output			
			Fuel Mass [g]	Char Mass (Reactor)		Gas (Dry, STP)		Condensate (Calculated)	
				[g]	[g]	[%]	[g]	[%]	[g]
2021-00078	500	7–10	470.3	120.7	25.7	71.5	15.2	278.0	59.1
2021-00079			490.1	126.6	25.8	74.5	15.2	289.1	59.0
2021-00084			458.8	118.3	25.8	65.9	14.4	274.6	59.9
2021-00108			480.5	124.2	25.8	65.2	13.6	291.1	60.6
2021-00122			485.6	127.5	26.3	70.2	14.4	288.0	59.3
2021-00210			490.2	122.6	25.0	71.3	14.5	296.3	60.4
2021-00213			476.9	124.7	26.1	67.4	14.1	284.8	59.7
2022-00027	850	12–13	481.3	105.4	21.9	93.6	19.4	282.3	58.6
2022-00028			463.5	101.2	21.8	89.8	19.4	272.6	58.8
2022-00040			461.1	101.3	22.0	93.0	20.2	266.8	57.9
2022-00041			475.2	104.6	22.0	98.3	20.7	272.3	57.3
2022-00057	850/900		481.2	101.6	21.1	88.0	18.3	291.6	60.6
2022-00065			470.1	101.9	21.7	84.0	17.9	284.2	60.5
2022-00134			466.7	98.1	21.0	84.1	18.0	284.5	61.0
2022-00138			463.3	101.4	21.9	85.0	18.3	276.9	59.8

Table 6. Total gas composition from 850 °C/900 °C pyrolysis and maximum calculated measurement error (2022-00057).

Gas	Volume Fraction [vol.%]	Maximum Error [vol.%]??
H ₂	38.7	±3.5
CO	26.6	±3.0
CH ₄	22.1	±3.4
CO ₂	11.9	±0.1
C ₂ H ₄	0.1	±2.4
C ₂ H ₆	0.6	±0.7

3.2. Char Powder Gasification

For gasification and combustion kinetics, studies report on several models to describe the char combustion. The approach with an Arrhenius-equation is commonly used and modified to obtain a fitting model equation [8]. Here an approximation also based on an Arrhenius equation was used similar to Gradel et al. to evaluate the parameters E_A , A_0 , and ν [4]. The following assumptions are made:

- the dependence on actual mass is of order zero in the first 25% of conversion;
- the reaction rate is chemically controlled without diffusion effects;
- a simple power law applies with respect to the reactive gas concentration;
- M_{char} is a hypothetical molar mass based on an ultimate analysis;
- $m_{0,char}$ is dry and ash free (daf).

Therefore, a zero-order approach for the solid fuel was used as shown in Equation (20).

$$\frac{dm_{t,char}}{dt} = -m_{0,char} M_{char} c_j^{\nu_{j,char}} A_{0,j,char} e^{-\frac{E_{A,j,char}}{T \cdot R}} \quad (20)$$

Morin et al. showed a list of kinetic expressions from former investigations of char combustion, such as those from Kashiwagi and Nambu [36] or Várhegyi, Sebestyén et al. [37], where dependence on the gas fraction is considered by partial pressure. Here, the gas concentration is used. The gas concentration is calculated by Equation (21).

$$c_j(T) = \frac{p_{amb}^{\nu_{f,j}}}{RT} \quad (21)$$

The experimental value evaluated is the mass fraction $F(t)$. To calculate $E_{A,j,char}$, $A_{0,j,char}$ and $\nu_{j,char}$ the change of mass fraction is used as described with Equation (22).

$$\frac{dF}{dt} = \frac{dm_{t,char}}{dt} \frac{1}{m_{0,char}} \quad (22)$$

Although the char was from a preliminary 850 °C pyrolysis, the TGA experiments show changes in mass during the first steps. Until step #4, a change due to evaporation of adsorbed water is assumed. Yet, a slight weight loss is additionally observed during the next heating phase with the investigated samples. This weight loss starts immediately with the heating step #4 at 130 °C and ends with step #5 when reaching T_{target} . The total weight loss during this period is 3–5 wt.% (of starting char mass). In the following stabilizing step #6, no weight loss occurs and a stagnation plateau can be observed. The weight loss until stagnation plateau dm_{stag} is used to calculate $m_{0,char}$ and $m_{t,char}$ where $m_{i,char}$ was the initial char mass:

$$m_{0,char} = m_{i,char} - dm_{stag} - m_{ash} \quad (23)$$

$$m_{t,char} = m_{i,char} - dm_{stag} - m_{ash} \quad (24)$$

Preliminary tests showed differences regarding the leftover ash in the TGA after a long reaction time with the different gases as listed in Table 7. Here, a standard deviation of up to 2.64 wt.% in ash content can be found. This may lead to an estimated total error of up to 6% in the evaluated value for $\frac{dF}{dt}$.

Table 7. Ash content after distinctive gas reactions in TGA and error due to ash content deviation on the evaluated reaction rate.

Gas	Ash-Content [wt. %]	SD [wt. %]	Estimated Possible dF/dt Error [%]
CO ₂	2.48	0.47	1.5
O ₂	4.14	0.97	2.5
H ₂ O	5.28	2.63	6

For the kinetic plots, $k_{j, \text{char}, \text{model}}$ was calculated as follows:

$$k_{j, \text{char}, \text{model}}(T) = A_{0, j, \text{char}} e^{-\frac{E_{A, j, \text{char}}}{T \cdot R}} \quad (25)$$

Logarithmic linear regression was used to evaluate $E_{A, j, \text{char}}$, $A_{0, j, \text{char}}$ by temperature variation and isolating $k_{j, \text{char}, \text{model}}$.

$$A_{0, j, \text{char}} e^{-\frac{E_{A, j, \text{char}}}{T \cdot R}} = -\frac{\frac{dF_{75}}{dt}}{c_j^{v_{j, \text{char}}} M_{\text{char}}} \quad (26)$$

Further, $v_{j, \text{char}}$ was evaluated with the established values for $E_{A, j, \text{char}}$, $A_{0, j, \text{char}}$ and the change of gas concentration in the experiments.

In Figure 12, the experimental data is shown. The “ $F_{\text{mod}, \text{chem}}$ ” line depicts the line for the evaluated model parameters from the first 25% of conversion without any limitation enhancements. Equation (27) is a model enhanced by a term based on the research for the random pore model of Bhatia and Perlmutter [38,39]. Here, a structural parameter Ψ_j is shown and may be described by Equation (28).

$$\frac{dF_{\text{mod}3}}{dt} = -M_{\text{char}} c_j^{v_{j, \text{char}}} A_{0, j, \text{char}} e^{-\frac{E_{A, \text{char}, j}}{R \cdot T}} F \sqrt{1 - \Psi_j \ln(F)} \quad (27)$$

$$\Psi_j = \frac{4\pi L_0(1 - \varepsilon_0)}{S_0^2} \quad (28)$$

Values for L_0 and S_0 were shown on a scale of $3 \times 10^6 \text{ cm cm}^{-3}$ and between 2×10^3 – $1.5 \times 10^5 \text{ cm}^2 \text{ cm}^{-3}$, respectively, by Bhatia and Perlmutter [38]. Yet, those values were not evaluated or applied in this study and the structural parameter Ψ_j was fitted by the least sum of squares for each reactive gas separately and only after evaluation of $E_{A, j, \text{char}}$, $A_{0, j, \text{char}}$ and $v_{j, \text{char}}$ which are shown in Table 8.

Table 8. Evaluated parameters for $E_{A, j, \text{char}}$, $A_{0, j, \text{char}}$ and $v_{j, \text{char}}$.

Gas, j	$A_{0, j, \text{char}}$	$E_{A, j, \text{char}}$	$v_{j, \text{char}}$
CO ₂	5.30×10^{13}	3.27×10^2	0.41
O ₂	5.79×10^7	1.32×10^2	0.61
H ₂ O	3.8×10^{10}	2.57×10^2	0.34

Since the experiments showed a significant change in reaction at around $F = 0.5$, an additional experiment with 1 mg powder instead of 2 mg was conducted to evaluate if the char powder height in the crucible or starting mass may be further influential. The experiment showed similar reaction behavior and only slightly faster decomposition, and thus assumed less influential as it was only half the starting mass.

In Figure 12A,E compared to Figure 12C, the curvature changes at around $F = 0.2$ and reaction takes place faster. In some cases, this is also later observed in particle measurements in Figure 14C in Section 3.3. While using least square fitting for Ψ_{CO_2} , it may cause a slightly higher value for Ψ_{CO_2} . In consequence, this may lead the model equation to a rate underestimation for $F \leq 0.2$ and a rate overestimation for $F \geq 0.2$.

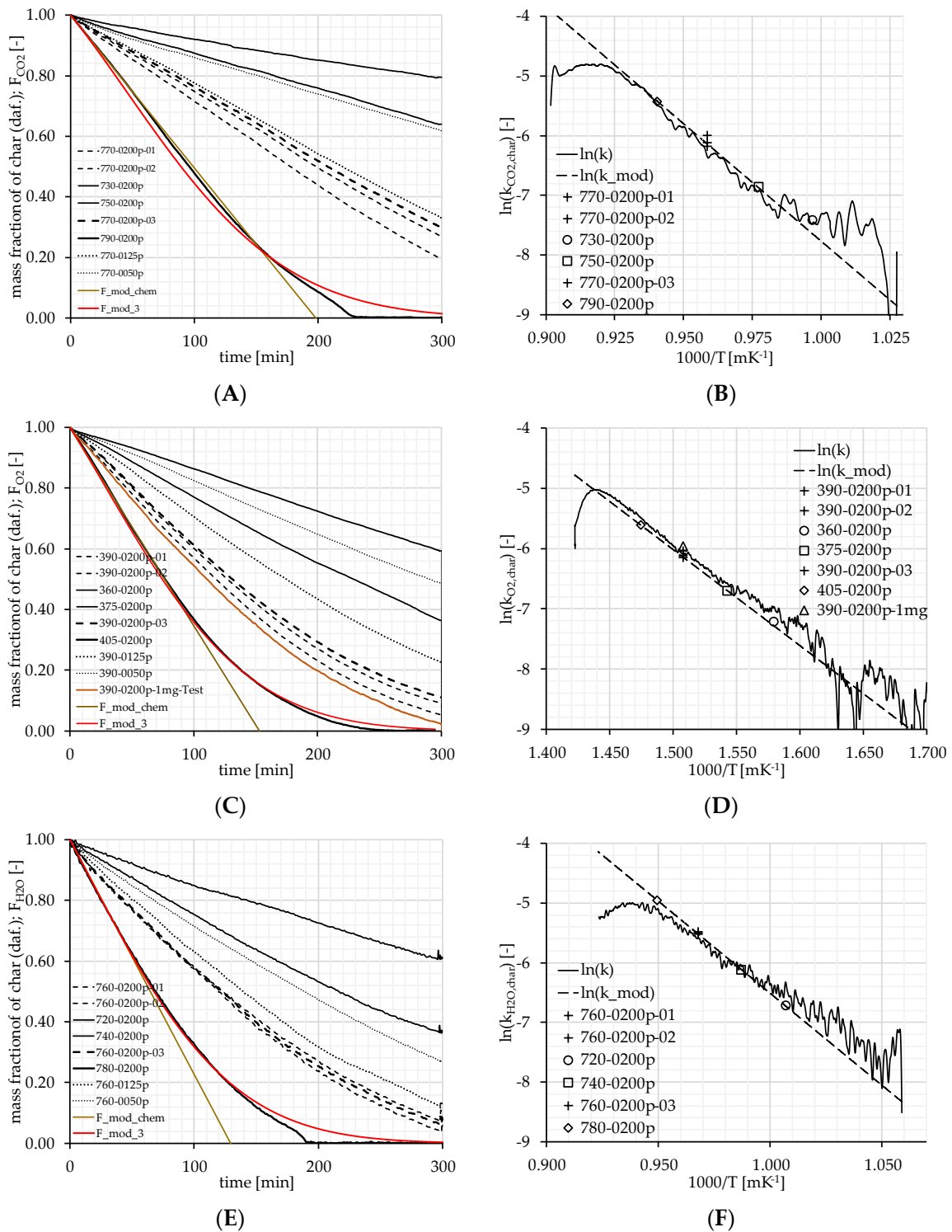


Figure 12. Results from TGA long-term experiments and Arrhenius-plots with rates from preliminary test measurements, points from TGA long-term experiments and the model line from established values of $E_{A,j,char}$, $A_{0,j,char}$ and $v_{j,char}$. F_{mod3} is a model approach (Form XXX-XXXXp indicates temperature in °C and $v_{f,j}$). (A) powder conversion with CO₂; $\Psi_{CO_2} = 4.8$; (B) Arrhenius plot CO₂; (C) powder conversion with O₂; $\Psi_{O_2} = 3.6$; (D) Arrhenius plot O₂; (E) powder conversion with H₂O; $\Psi_{H_2O} = 2.5$; (F) Arrhenius plot H₂O.

3.3. Single Particle Char Gasification

Particle reaction and powder reaction are compared in Figure 13, where powder reaction is calculated by Equation (25) and the effective limitation $k_{char,j,eff}$ is calculated and applied by Equation (19). To achieve the appropriate limitation with Equation (17b), a tentative correction factor of $\omega_{cf} = 10$ was introduced. Without this factor, $k_{char,j,chem}$ and $D_{j,eff}$ are key influential parameters under the square root. Yet, $k_{char,j,chem}$ was evaluated by experiments and $D_{j,eff}$ was calculated by Equation (16) and showed good agreement in the former investigations [4,34]. The correction factor is further discussed in Section 4. The influence of d_p is depicted by two dashed lines with lower and upper boundaries of d_p for comparison purpose. Since the standard deviation of the reaction rate in particle measurements is around $\pm 20\%$, these totaling 40% are roughly depicted by the spread of lines and thus show the significant influence of d_p as a particle size parameter.

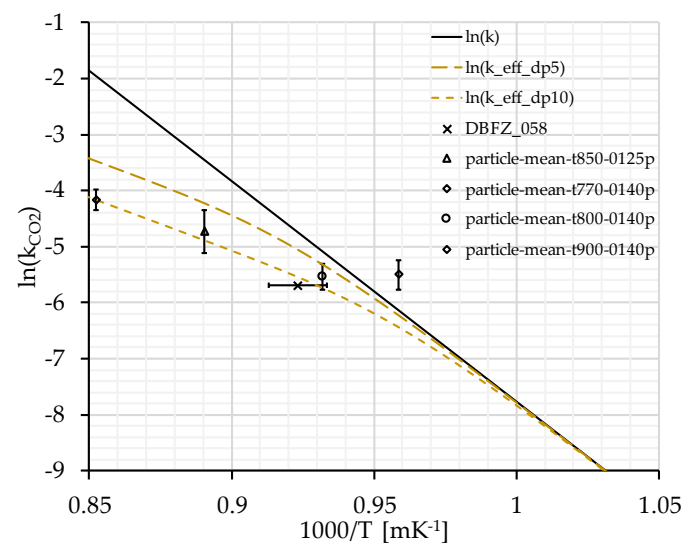


Figure 13. Arrhenius plot of CO₂ measurements. Black line depicts resulting rate from long-term powder measurements with $E_{A,CO_2,char}$, $A_{0,CO_2,char}$. The dashed brown lines show the used limitation function for diffusion with a lower and upper value of the influencing particle diameter ($d_{p,low} = 0.005$ m; $d_{p,up} = 0.010$ m) and an applied correction factor of $\omega_{cf} = 10$. Single points show the average rate of particle measurements with standard deviation. The cross indicates an estimated mean temperature in the fixed-bed batch reactor CO₂ measurement with a horizontal error indicator showing the deviation in temperature.

The rate evaluated in batch measurements of the DBFZ is assumed with an average temperature of 810 °C with a standard deviation of 12 °C depicted horizontally. Here, particle measurements with 800 °C and $v_{f,CO_2} = 0.14$ already show a higher reaction rate. Thus, this underlines a significant gap between single particle and bulk measurements.

The measurement of particles at 770 °C on the gridded sample carrier showed higher reaction rates than the supposed chemically controlled reaction rate by powder measurements. Yet, the mean particle reaction rate at 770 °C was higher by a factor of two. Some particle rates were higher by a factor of three. Also, the particle measurements at 770 °C show higher rates than those at 800 °C.

Figure 14A–C shows the mass fraction during experiments. Here, the differences become clearer to see as the particles react quite differently. Some particles show a stronger decomposition at the beginning and tend to a lower reaction rate in the end, and vice versa. Thus, the divergence in reaction rate for a single particle tends to narrow close to full conversion in some cases. Anyways, the reaction rate after a conversion of 0.25 was used for comparison of particle and powder measurements.

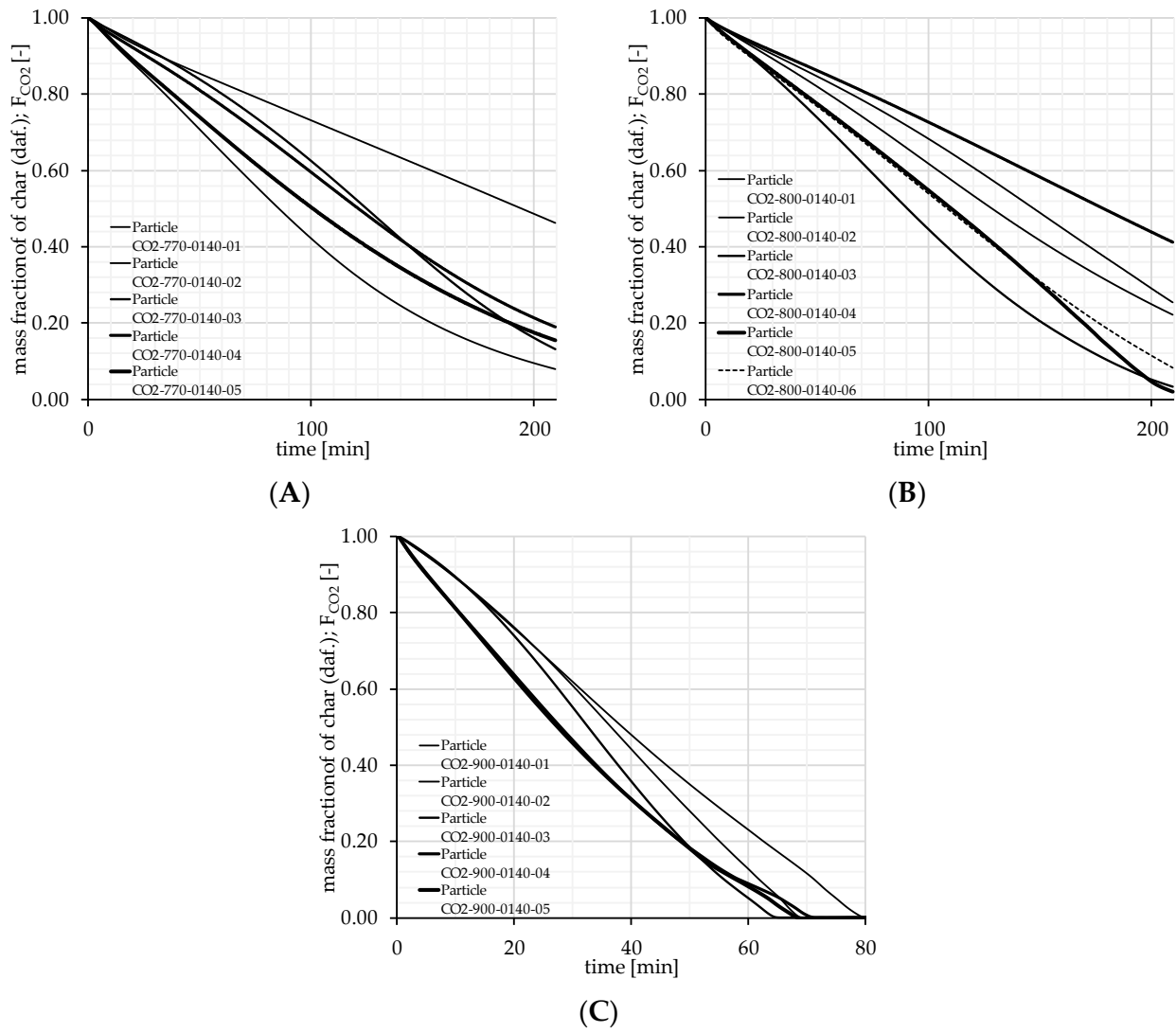


Figure 14. Mass fraction of char during particle measurements $v_{f,CO_2} = 0.14$ with different particle mass and size at 770 °C, 800 °C and 900 °C in (A–C), respectively. Particle details are provided in Tables 9–11 below.

Table 9. Details on the particles used in measurements at 770 °C.

Particle	Approx. Size [mm]			Volume [mm ³]	Weight [mg]	$\frac{dX_{25}}{dt}$ [$\times 10^{-5} \text{ s}^{-1}$]	Approx. $\rho_{c,0}$ [kg m ⁻³]
	L	W	H				
01	7	7	3.2	156.8	29.5	4.57	245
02	8.9	5.9	4.2	220.5	36.6	9.75	151
03	9.2	7.8	2.9	208.1	23.9	5.89	102
04	9.7	7.5	3	218.3	33.1	6.56	395
05	12.7	7	3.5	311.2	58.8	8.44	198
Avg.	9.5	7.0	3.4	223.0	36.4	7.04	162
Std.dev.	1.8	0.7	0.5	49.8	12.0	1.84	27

Table 10. Details on the particles used in measurements at 800 °C.

Particle	Approx. Size [mm]			Volume [mm ³]	Weight [mg]	$\frac{dX_{25}}{dt}$ [$\times 10^{-5} \text{ s}^{-1}$]	Approx. $\rho_{c,0}$ [kg m ⁻³]
	L	W	H				
01	6.9	5.3	3.3	120.7	29.6	5.17	245
02	10.5	7.1	2.7	201.3	30.4	6.18	151
03	10	7.5	5.5	412.5	41.9	8.68	102
04	7.2	7	2.4	121.0	47.8	4.56	395
05	9	8.2	3.5	258.3	51.2	7.19	198
06	7.1	6.8	4.1	198.0	47.1	8.02	238
Avg.	8.5	7.0	3.6	218.6	41.3	6.63	222
Std.dev.	1.5	0.9	1.0	99.2	8.5	1.47	92

Table 11. Details on the particles used in measurements at 900 °C.

Particle	Approx. Size [mm]			Volume [mm ³]	Weight [mg]	$\frac{dX_{25}}{dt}$ [$\times 10^{-5} \text{ s}^{-1}$]	Approx. $\rho_{c,0}$ [kg m ⁻³]
	L	W	H				
01	8.5	6.2	2.8	147.6	28.7	20.7	195
02	6.7	6.6	3.2	141.5	28.3	20.6	200
03	8	6.1	3.9	190.3	25.1	22.9	132
04	6.9	5.4	3.5	130.4	21.6	30.4	166
05	5.5	5.1	2.8	79.5	15.4	31.0	196
Avg.	7.1	5.9	3.2	137.7	23.8	25.1	178
Std.dev.	1.1	0.6	0.4	36.9	4.9	4.65	26

3.4. Fixed-Bed Batch Char Gasification and Model Comparison

The char pyrolyzed at 850 °C/900 °C was used for the CO₂ gasification in the DBFZ fixed-bed reactor (Section 2.4). Figure 15 shows a characteristic profile of the measured product gas. After switching from the N₂ to N₂/CO₂ mixture (86 vol.%/14 vol.%) at the reactor inlet, a stable gas mixture of 11 vol.% of CO and 5.5 vol.% of CO₂ is established in the product gas.

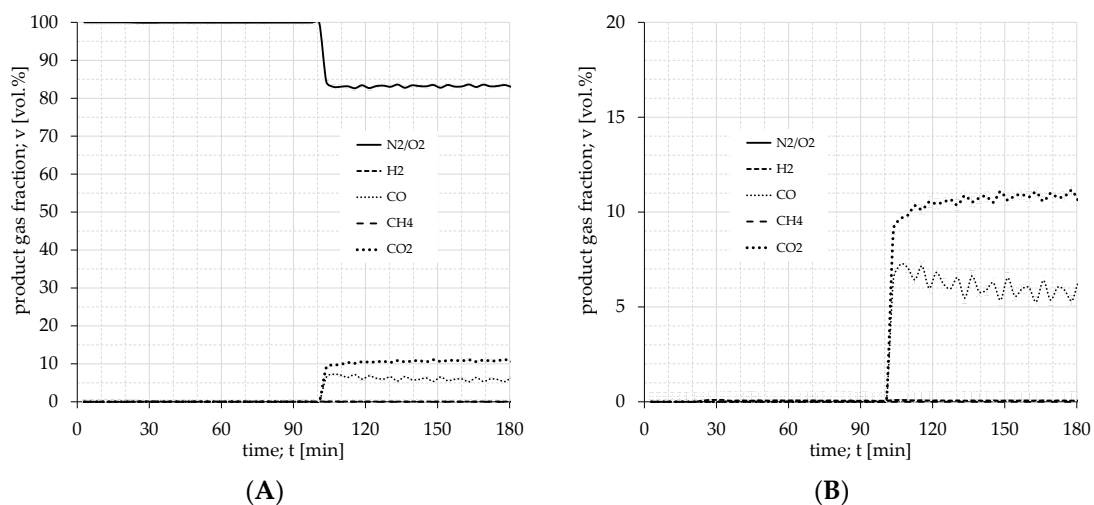


Figure 15. Product gas concentration of CO₂ gasification (2022–00058) of pyrolysis char (2022–00058). (A) Gas composition scaled with N₂ and (B) scaled to values of CO₂ and CO.

The CO₂ gasification mass balances are shown in Table 12. The table shows 65–72% of the pyrolysis char mass remains in the reactor after the reaction as gasification char. The other part of the pyrolysis char enters the product gas through the 80 min gasification reaction. The mass balance agreed with the measurement results. Measurement errors or deviations in the mass balance in the range of 1% result from the lack of measurement of the product gas moisture and pyrolysis reaction in the non-measurable range.

Table 12. CO₂ gasification products at different temperatures and a heating rate of 7–10 K min^{−1}.

Experiment Number	Pyrolysis Temperature [°C]	Heating Ratio [K min ^{−1}]	Input				Output			
			Fuel Mass (Reactor)	Gasification Agent	Σ _{in}	Σ _{out}	Char Mass (Reactor)	Gas (Dry, STP)		
			[g]	[g]	[g]	[g]	[g]	[%]	[g]	[%]
2022-00047	850	31–34	102.6 (2022-00041)	431.2	533.8	529.6	66.4	64.7	463.2	35.3
2022-00048			99.4 (2022-00040)	419.1	518.5	513.3	67.2	67.6	446.1	32.8
2022-00058			101.1 (2022-00057)	428.8	529.9	529.9	72.0	71.2	457.9	28.8
2022-00126			99.0 (2022-00065)	446.1	545.1	542.8	70.9	71.6	471.9	28.4

The mass balance for the gasification reaction inside the DBFZ fixed-bed reactor can be established in the experimental period for the various experiments. Table 13 shows such a reactor mass balance for the experiment 2022–00058, with a maximal measurement error calculation.

Table 13. Reactor mass balance for experiment 2022–00058 with maximum measurement error calculation.

Input Mass		Min [g]	Measurement Amount [g]	Max [g]
Material	Measurement Error			
fuel	±0.1%	101.01	101.11	101.21
feed gas CO ₂	±0.23 L h ^{−1} at 100 L h ^{−1} STP	428.15	428.81	429.46
feed gas N ₂	±10.83 L h ^{−1} at 1000 L h ^{−1} STP	1643.67	1663.08	1682.51
	Σ input	2172.83	2193.00	2213.18
	Σ input without N ₂	529.16	529.92	530.67
	output mass			
char	± 2%	70.55	71.99	73.43
product gas		2028.70	2124.56	2227.15
product gas without N ₂		439.56	457.92	483.01
condensate (tar, water)	-	not measured	not measured	not measured
	Σ output	2099.25	2196.55	2300.58
	Σ output without N ₂	510.11	529.91	556.44
	balance			
	output – input	−73.58	3.55	87.40
		−3.39% of input mass	0.16% of input mass	3.95% of input mass
	output – input (without N ₂)	−19.05	−0.01	25.77
		3.60% of input mass	<0.002% of input mass	4.86% of input mass

The target of the CO₂ gasification experiments was to investigate or characterize the reaction of carbon (C) with carbon dioxide (CO₂) to carbon monoxide (CO). For the experiment 2022-00058, this reaction can be represented based on the measured values as shown in Table 14. The pyrolysis char reacts with CO₂ as expected according to the theory, while the mass balance of the reaction could be closed by measured values. Thus, the measured values obtained can be used to compare the simulation model.

Table 14. CO₂ reaction mass balance for experiment 2022-00058.

Measured CO ₂ Gasification Reaction					
	C	+	CO ₂	<->	2 CO
	1 mol	+	1 mol		2 mol
	29.12 g		93.32 g		122.33 g
					Σinput 122.44 g
					-0.11 g (0.37% _{C-reaction})
mass calculation					
	101.01 g	-	71.99 g char output	=	29.12 g C reaction
	char input				
	428.80 g CO ₂	-	335.48 CO ₂ product gas	=	93.32 g CO ₂ reaction
	feed gas				

To evaluate and compare the results of the model and the gasification in the laboratory reactor, the gas fraction of CO₂ and CO are compared at the outlet in Figure 16B. Additionally, the residual char after the experimental time of roughly 90 min is used as an indicator. The experimental data shows a higher CO output and thus reaction rate in the beginning, decreasing during the experiment. Hence, the model may correlate more strongly to the given temperature than the experimental data from the laboratory reactor.

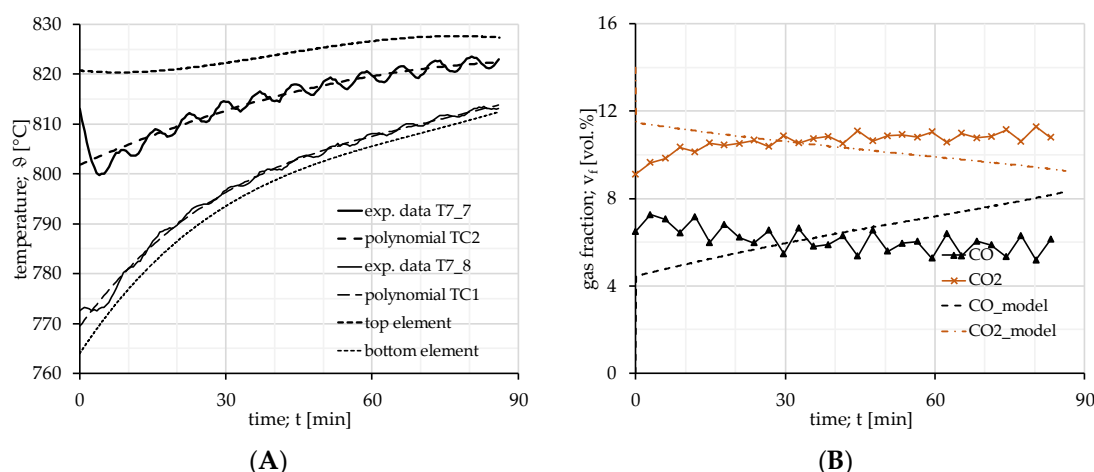


Figure 16. Comparison of experimental and model data for the laboratory batch reactor experiments: (A) temperature measured, polynomials used and extrapolated bottom and top element temperature; (B) gas fraction measured at the outlet and values at the model outlet.

Figure 16A shows the temperatures measured in the reactor, temperatures modeled by polynomials (5) and (6), and the extrapolated temperatures at the bottom and the top element in the model. The upper thermocouple (T7_7) shows a temperature reduction of 15 K in the first five minutes of the experiment indicating a stronger reaction and therefore cooling by endothermic reaction. The temperature rises as the experiment progresses. The lower thermocouple (T7_8) begins at 773 °C and ends at 813 °C. The fluctuation in temperature is due to the regulation of the heating system.

Figure 17 depicts the modeled volume fraction of gas throughout the reactor bed at the end of the experimental time and indicates a slightly decreasing reaction rate at the reactor end. The experimental residual mass was a mass fraction of 71.2% after 5171 s.

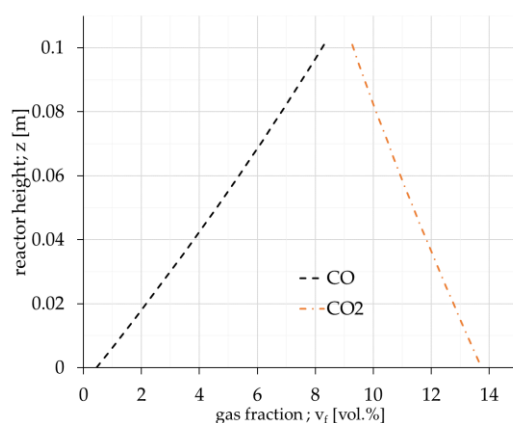


Figure 17. Calculated gas composition of CO and CO₂ in the reactor bed at the end of the experimental time of 5171 s.

Figure 18A analyzes the model sensitivity using the Sauter diameter of 0.0076 m as a reference. With the assumed temperature profile in the model, the previously used correction factor of $\omega_{cf} = 10$ for matching the particle measurements is insufficient in describing the reaction in the bulk. Here, a stronger limitation is needed than solely the model for external and internal particle diffusion. In this case, ω_{cf} would have to be of a magnitude of 15. However, the used correction factor is a link to the physical properties for pore diffusion and not to those of the bulk. Thus, there is yet a missing factor between the particle and bulk measurements. A conversion of 39% in the model compared to a conversion of 29% in the experiment shows that the reaction rate needs a further bulk limitation of about the factor 0.75. Figure 18B shows the model sensitivity for changing values of d_p with $\omega_{cf} = 10$. Changing d_p in the range from 5 mm to 9 mm and ω_{cf} from 10 to 18 shows an impact of up to 15% in total on the residual mass fraction after an experimental time of 5171 s.

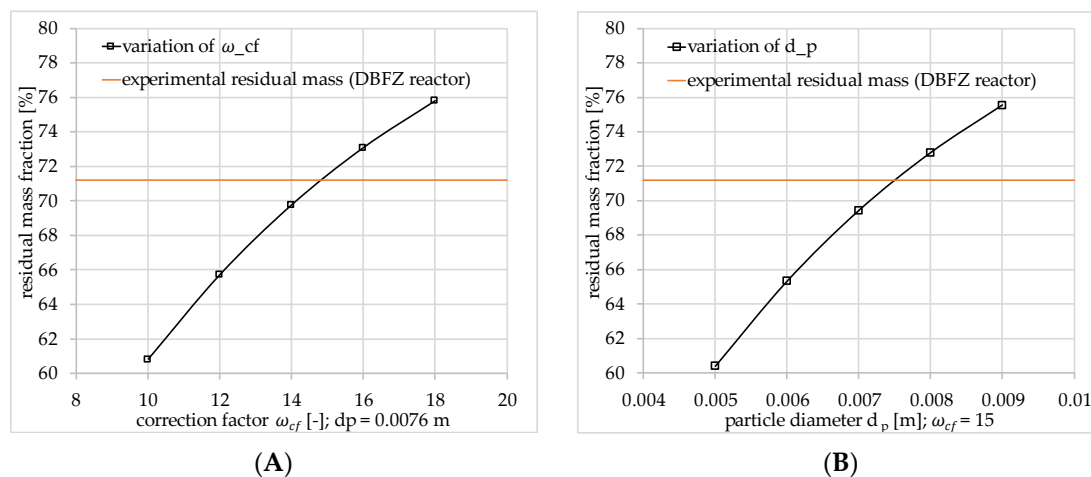


Figure 18. (A) Residual mass fraction calculated by model variation of parameters ω_{cf} and (B) d_p ; orange line indicates the measured residual mass from the bulk experiment.

3.5. Discussion

The pyrolysis products in this study are 21–22 wt.% residual char, 57.3–60.6 wt.% condensate, and 17.9–20.7 wt.% gas, as shown in Table 6. A possible comparable data set for spruce pyrolysis is provided by Anca-Couce et al. [40]. It is important to consider that the heating rate is 60 K min⁻¹ and the biomass is pelletized in their research. The closest comparison is the pyrolysis between 650 °C and 750 °C due to seemingly uncracked tar compared to 950 °C. While the amount of H₂ is not shown, the mass fractions of CO, CO₂,

CH₄, condensate (H₂O and tar), and char are compared in Table 15. Some values like condensate and total gas are matching at 650 °C while others like CH₄ do so at 750 °C. Also, some values for pine (as another softwood) are listed by Grieco and Baldi [41] with a heating rate of 3 K min⁻¹ and 703 °C in pyrolysis. Overall, the total fractions of char, condensate and gas are in a similar range as in the literature. Due to different pyrolysis conditions, the gas fractions may vary. However, the measurement equipment was calibrated before and after the pyrolysis in this study for valid data.

Table 15. Comparison of pyrolysis products with the literature in wt.% of solid fuel.

Component	Mass Fraction [wt.% to Fuel]			
	This Study	650 °C [40]	750 °C [40]	703 °C Pine [41]
char	21.5	15.6	15.0	27
condensate	58.9	61.5	48.9	54
thereof H ₂ O	-	19.2	15.9	20
total gas	19.3	22.1	34.6	21
H ₂	0.87	-	-	0.2
CO	8.34	7.7	20.3	6.0
CH ₄	3.96	1.6	3.8	2.3
CO ₂	5.60	12.3	9.3	11.5
C ₂ H ₄	0.03	0.5	1.2	-
C ₂ H ₆	0.20	-	-	-

An explicit comparison of the evaluated parameters, $E_{A,j,char}$, $A_{0,j,char}$ and $v_{j,char}$ for the proposed model with previous studies is limited. Multiple factors like char types, particle sizes, experimental methods, evaluation routines, and more are difficult to match. Di Blasi found throughout various literature a strong deviation as shown in Table 16 [42]. The deviation can be partly explained by multiple factors previously named. In this study, the order v_j refers to the gas concentration while some refer to partial pressure and some to neither. Therefore, the unit of the preexponential factor A_0 varies as well. Comparing the evaluated combustion parameters, this study shows agreement within the range shown in the literature. The H₂O gasification parameters of this study seem only slightly out of range. For CO₂ gasification, the parameters are far more out of range, although the evaluation routine is equal to the ones with the other reactive gas agents. Exemplarily, Schneider et al. also reported parameters for CO₂ gasification slightly outside the range compared herein for high temperature pyrolyzed beech wood (>1400 °C) with a power law model [43].

Table 16. Comparison of gasification parameters with various literature data.

Parameter	This Study	Various Research Reviewed by Di Blasi [42]	Schneider et al. [43]	Unit
E_{A,CO_2}	3.27	0.88–2.50	3.0–3.1	[$\times 10^2$ kJ/mol]
A_{0,CO_2}	5.30×10^{13}	3.1×10^6 – 2.59×10^8	5.68×10^9 – 1.02×10^{10}	varying
v_{CO_2}	0.41	0.4–0.6	0.19–0.21	-
E_{A,O_2}	1.32	0.76–2.29	-	[$\times 10^2$ kJ/mol]
A_{0,O_2}	5.79×10^7	5.3×10^5 – 4.5×10^8	-	varying
v_{O_2}	0.61	0.5–1	-	-
E_{A,H_2O}	2.57	1.43–2.37	2.35–2.64	[$\times 10^2$ kJ/mol]
A_{0,H_2O}	3.8×10^{10}	1.7×10^5 – 2.62×10^8	1.55×10^6 – 5.7×10^8	varying
v_{H_2O}	0.34	0.4–1	0.45–0.47	-

Further in 2022, Trubetskaya reviewed the influence of inorganic content in biomass on gasification rates with a view to investigating inorganic elements in combination with

reaction rates [44]. Therefore, the inorganic elements for the analyzed biomass can be found in Appendix A.

Single particle experiments showed limited reaction behavior at temperatures of 800 °C, 850 °C and 900 °C compared to powder measurements with the exception of 770 °C. Here, the particle reaction rate was higher. This may indicate better access of the reactive gas to the internal char surface of a particle at particles on the meshed sample carrier than to the char powder in the crucible on the DSC sample carrier.

Yet, surprising were the results of single particles reacting at faster or similar rates at 770 °C than those at 800 °C in a CO₂ atmosphere. A hypothesis may be that in this temperature range, the transition between the accessible internal surface and evolving reaction layer occurs. The product gas begins to block the reactive gas from access to deeper pore structure while at 770 °C; due to slower local reaction, the reactive gas may still access more internal surfaces and spread more evenly throughout the whole particle leading to a similar or even faster reaction. Additionally, because of less local accumulation of product gas near the outer particle surface, there might be a better gas exchange inside the particle. Hence, a future field of interest may be to explain this transitional behavior more precisely.

Further investigation must be made due to the tentative correction factor ω_{cf} . This work priority assumed no Knudsen regime to be present and thus no influence of pore diameter d_{pore} . Knudsen regime occurs at $d_{pore} \leq 10$ nm, and adds the pore diameter dependency to $D_{j,mix}$ with D_{Knu} as found in descriptions by Jess and Wasserscheid [32]. Thus, the calculation of D_{pore} may be enhanced as follows:

$$D_{pore} = \left(\frac{1}{D_{j,N_2}} + \frac{1}{D_{Knu}} \right)^{-1} \quad (29)$$

with

$$D_{Knu} = \frac{1}{3} \sqrt{\frac{8RT}{\pi M}} d_{pore} \quad (30)$$

Pore structure and thus diameter may vary depending on type of biomass char, pyrolysis conditions and further along different conversion levels of the biomass char. A comparison with yet unvalidated BET-data showed average d_{pore} values of magnitude 1–4 nm. Former investigations by Gradel [35] on wood pellets showed values of 2.5 nm. Using D_{Knu} with these pore diameters in the limitation function (17a) may achieve its purpose without ω_{cf} for single particle predictions. Hence, more profound BET-data must be acquired, and investigations made for the used biomass and others.

In 2020, Wu et al. showed related parameters evolving during conversion like micro-pore area, external surface area and porosity [45]. Their research covers higher volume fractions of CO₂ (0–90%) and H₂O (0–50%) in temperature ranges of 1150–1350 °C with poplar wood, switch grass and corn stover. Liang and Singer used detailed 3-D CFD modeling and X-ray micro-computed tomography with high resolution on single particle bituminous coal combustion to assess the limitation and effectiveness factors for 1-D reactor modeling with data of pore structure [46]. Research of Nguyen et al. showed similar detailed particle modelling in 2021 [47]. Their CFD model involves a detailed description for a spherical particle and the evolving morphology during char conversion using likewise data for pore structure and gasification kinetics. Thus, representative particle size for a specific biomass bulk must be determined as well as the description of pore structure by representative values of specific surface area, porosity, and pore diameter.

However, the bulk measurements on the laboratory scale show an even lower overall reaction rate by a factor of 0.75 compared to single particle reaction, although good purging with reactive gas was achieved in the laboratory fixed-bed batch reactor, which is why corrections and therefore further investigation must be made. Additionally, these differences may be investigated with H₂O, O₂ and combinations as well.

4. Conclusions

This work aims to produce wholesome combined data for modeling thermal fixed-bed gasification with biomass-specific data evaluated in small-scale laboratory measurement routines. Thus, many properties of the investigated biomass are provided and reproducible pyrolysis data is presented. TGA measurements of fine char powder were conducted, in a controlled regime below 800 °C to evaluate the reaction parameters, $E_{A,j,char}$, $A_{0,j,char}$ and $v_{j,char}$ for reactive gases CO₂, O₂, and H₂O for the use in the proposed model. Additionally, single particle and bulk gasification in a CO₂ atmosphere were investigated for the limitation modeling and model validation. The particle measurement showed similar reaction rates at 770 °C and 800 °C. Furthermore, at 770 °C, the particle reaction rate was higher than the evaluated powder reaction rate in a controlled regime. Thus, supplementary investigations are needed to describe those phenomena.

Recent detailed particle simulation may benefit from a reliable database of biomass-specific characteristics such as reaction parameters or pore structure. Yet, the suitability of this study for different models must be determined. More pore structure measurements must be conducted since the Knudsen regime and thus pore diameter is significant for biomass char. Sophisticated simulation models with reliable biomass data can provide efficient and adaptable predictions to enhance the development of industrial gasification and make greater use of the biomass spectrum.

Supplementary Materials: Supporting information will be provided under the following depository link: <https://www.mdpi.com/article/10.3390/en16062888/s1>.

Author Contributions: Conceptualization, M.R.H., A.H., A.G., M.K. and T.P.; data curation, M.R.H. and A.H.; formal analysis, M.R.H. and A.H.; funding acquisition, T.P.; investigation, A.H.; methodology, M.R.H. and A.H.; project administration, T.P.; software, M.R.H. and A.G.; supervision, M.K. and T.P.; validation, M.R.H. and A.H.; visualization, M.R.H. and A.H.; writing—original draft, M.R.H.; writing—review & editing, M.R.H., A.H., A.G., M.K. and T.P. All authors have read and agreed to the published version of the manuscript.

Funding: This research and APC was funded by Federal Ministry for Economic Affairs (Germany) and Climate Action, grant number “03KB163A” (Bundesministerium für Wirtschaft und Klimaschutz BMWK).

Institutional Review Board Statement: Not applicable.

Informed Consent Statement: Not applicable.

Data Availability Statement: The data presented in this study are available on request from the corresponding author. The data are not publicly available due to English language preparation and distinguishing from other private data evaluation, yet. Any requested material will be publicly provided here: <https://nextcloud.hof-university.de/s/zjtBsGJHYQaRQ9N>.

Conflicts of Interest: The authors declare no conflict of interest. The funders had no role in the design of the study; collection, analyses, or interpretation of data; writing of the manuscript; or decision to publish the results.

Nomenclature

	Symbols Used	Unit
A_0	preexponential factor	$\text{m}^3 \text{kg}^{-1}$
c	molar concentration	mol m^{-3}
c_p	heat capacity	$\text{J kg}^{-1} \text{K}^{-1}$
d, d_i	diameter, inner diameter	M
D	diffusion coefficient	$\text{m}^2 \text{s}^{-1}$
E_A	activation energy	kJ mol^{-1}
F	residual mass fraction	-

h	height	m
H	reaction enthalpy	J mol ⁻¹
l	length	m
L ₀	total length of overlapped system per unit volume	cm cm ³
M	molar mass	kg mol ⁻¹
n	number	-
Nu	Nusselt number	-
p ₀	atmospheric pressure	kg m ⁻¹ s ⁻²
Q	heat flow	-
r	reaction rate	mol s ⁻¹ m ⁻³
R	gas constant	J kg ⁻¹ mol ⁻¹
Re	Reynolds number	-
S	surface area	m ²
S ₀	inner surface area per unit volume at t=0	cm ² cm ³
S _{p,o}	outer surface area per unit mass of particle	m ² kg ⁻¹
Sc	Schmidt number	-
Sh	Sherwood number	-
t	time	s
T	absolute temperature	K
U	velocity	m s ⁻¹
v _f	volume fraction	-
w	mass fraction	-
$\bar{x}_{1,2}$	Sauter diameter	m
X	conversion	-
z	coordinate	m
	Sub- and Superscripts	Unit
0	at the beginning	
bm	biomass	
chem	chemically	
char	investigated char	
eff	effective	
g	gas	
i	indicator solid species; numerical time step	
j	indicator gaseous species	
n	numerical element step	
p	particle	
pyr	pyrolysis	
s	solid	
t	time dependent	
TC	thermocouple	
total	e.g., total porosity	
w	wall	
	Greek Letters	
β	mass transfer coefficient	m s ⁻¹
γ	mass concentration	kg m ⁻³
ϵ	porosity	m _g ³ m ⁻³
φ	structure factor	-
ϕ	Thiele modulus	-
ν	reaction order	-
ρ	density	kg m ⁻³
τ	tortuosity	-
λ	heat conductivity	W m ⁻¹ K ⁻¹
η	effectiveness factor	-
θ	temperature	°C
Ψ	structural factor	-
ω_{cf}	correction factor	-

	Abbreviations
n.d.	not detectable
ASC	automatic sample changer
DSC	differential scanning calorimetry
DWC	defined wooden chips
daf	dry ash free
FTIR	Fourier-transform infrared spectroscopy
ICP-OES	inductively coupled plasma optical emission spectrometry
μ GC	micro gas chromatography
MFC	mass flow controller
SD	standard deviation
TGA	thermogravimetric analysis

Appendix A

Table A1. ICP–OES results of biomass and char with 24 listed elements.

Element	Amount [mg kg^{-1} (Dry)]	
	Spruce	Char
Aluminum	4.35	34
Barium	27.6	86.2
Cadmium	0.375	n.d.
Calcium	1150	3060
Chrome	0.642	3.88
Cobalt	0.399	0.202
Copper	0.904	3.27
Iron	15.1	49.6
Lead	n.d.	n.d.
Lithium	n.d.	n.d.
Magnesium	160	480
Mangan	350	603
Molybdenum	n.d.	n.d.
Nickel	0.662	5.53
Phosphorus	48.5	192
Potassium	260	1570
Silicon	48.2	n.d.
Sodium	n.d.	41.3
Strontium	7.17	20.3
Sulfur	84.4	94.9
Thallium	n.d.	n.d.
Titanium	0.881	8.95
Tungsten	n.d.	n.d.
Zinc	16.8	37.5

References

1. Sikarwar, V.S.; Zhao, M.; Clough, P.; Yao, J.; Zhong, X.; Memon, M.Z.; Shah, N.; Anthony, E.J.; Fennell, P.S. An overview of advances in biomass gasification. *Energy Environ. Sci.* **2016**, *9*, 2939–2977. [[CrossRef](#)]
2. Anca-Couce, A. Reaction mechanisms and multi-scale modelling of lignocellulosic biomass pyrolysis. *Prog. Energy Combust. Sci.* **2016**, *53*, 41–79. [[CrossRef](#)]
3. Di Blasi, C. Heat, momentum and mass transport through a shrinking biomass particle exposed to thermal radiation. *Chem. Eng. Sci.* **1996**, *51*, 1121–1132. [[CrossRef](#)]
4. Gradel, A.; Honke, R.; Wüning, J.A.; Plessing, T.; Jess, A. Modeling of Biomass Gasification in a Downdraft Gasifier with Integrated Tar Adsorption. *Chem. Eng. Technol.* **2019**, *42*, 1895–1906. [[CrossRef](#)]
5. Kaltschmitt, M.; Hartmann, H.; Hofbauer, H. *Energie aus Biomasse: Grundlagen Techniken und Verfahren*, 3rd ed.; Springer: Berlin/Heidelberg, Germany, 2016; ISBN 978-3-662-47437-2.
6. Basu, P. Gasification Theory. In *Biomass Gasification, Pyrolysis and Torrefaction: Practical Design and Theory*, 3rd ed.; Basu, P., Ed.; Academic Press: London, UK, 2018; pp. 211–262. ISBN 9780128129920.
7. Neves, D.; Thunman, H.; Matos, A.; Tarelho, L.; Gómez-Barea, A. Characterization and prediction of biomass pyrolysis products. *Prog. Energy Combust. Sci.* **2011**, *37*, 611–630. [[CrossRef](#)]

8. Morin, M.; Pécate, S.; Masi, E.; Hémati, M. Kinetic study and modelling of char combustion in TGA in isothermal conditions. *Fuel* **2017**, *203*, 522–536. [[CrossRef](#)]
9. Guerrero, M.; Ruiz, M.P.; Alzueta, M.U.; Bilbao, R.; Millera, A. Pyrolysis of eucalyptus at different heating rates: Studies of char characterization and oxidative reactivity. *J. Anal. Appl. Pyrolysis* **2005**, *74*, 307–314. [[CrossRef](#)]
10. Cetin, E.; Moghtaderi, B.; Gupta, R.; Wall, T. Influence of pyrolysis conditions on the structure and gasification reactivity of biomass chars. *Fuel* **2004**, *83*, 2139–2150. [[CrossRef](#)]
11. Kumar, M.; Gupta, R.C. Influence of carbonization conditions on the gasification of acacia and eucalyptus wood chars by carbon dioxide. *Fuel* **1994**, *73*, 1922–1925. [[CrossRef](#)]
12. Fushimi, C.; Araki, K.; Yamaguchi, Y.; Tsutsumi, A. Effect of Heating Rate on Steam Gasification of Biomass. 1. Reactivity of Char. *Ind. Eng. Chem. Res.* **2003**, *42*, 3922–3928. [[CrossRef](#)]
13. Mermoud, F.; Salvador, S.; Vandesteene, L.; Golfier, F. Influence of the pyrolysis heating rate on the steam gasification rate of large wood char particles. *Fuel* **2006**, *85*, 1473–1482. [[CrossRef](#)]
14. Okumura, Y.; Hanaoka, T.; Sakanishi, K. Effect of pyrolysis conditions on gasification reactivity of woody biomass-derived char. *Proc. Combust. Inst.* **2009**, *32*, 2013–2020. [[CrossRef](#)]
15. Zanzi, R.; Sjöström, K.; Björnbom, E. Rapid high-temperature pyrolysis of biomass in a free-fall reactor. *Fuel* **1996**, *75*, 545–550. [[CrossRef](#)]
16. Morin, M.; Pécate, S.; Hémati, M.; Kara, Y. Pyrolysis of biomass in a batch fluidized bed reactor: Effect of the pyrolysis conditions and the nature of the biomass on the physicochemical properties and the reactivity of char. *J. Anal. Appl. Pyrolysis* **2016**, *122*, 511–523. [[CrossRef](#)]
17. Irfan, M.F.; Usman, M.R.; Kusakabe, K. Coal gasification in CO₂ atmosphere and its kinetics since 1948: A brief review. *Energy* **2011**, *36*, 12–40. [[CrossRef](#)]
18. Federal Ministry of Food and Agriculture. Holzmarktbericht 2021: Abschlussergebnisse für die Forst- und Holzwirtschaft des Wirtschaftsjahres. 2021. Available online: <https://www.bmel-statistik.de/forst-holz/holzmarkt/holzmarktberichte> (accessed on 7 March 2023).
19. ICS 75.160.40 (DIN EN ISO 16948); Solid Biofuels—Determination of Total Content of Carbon, Hydrogen and Nitrogen. Beuth Verlag GmbH: Berlin/Heidelberg, Germany, 2015.
20. ICS 75.160.40 (DIN EN ISO 16967:2015); Solid Biofuels—Determination of Major Elements. Beuth Verlag GmbH: Berlin/Heidelberg, Germany, 2015.
21. ICS 75.160.40 (DIN EN ISO 16968); Solid Biofuels—Determination of Minor Elements. Beuth Verlag GmbH: Berlin/Heidelberg, Germany, 2015.
22. ICS 75.160.40 (DIN EN 14775); Solid Biofuels—Determination of Ash Content. Beuth Verlag GmbH: Berlin/Heidelberg, Germany, 2012.
23. ICS 75.160.10 (DIN 51719); Testing of Solid Fuels—Solid Mineral Fuels—Determination of Ash Content. Beuth Verlag GmbH: Berlin/Heidelberg, Germany, 1997.
24. ICS 75.160.40 (DIN EN 14774-2); Solid Biofuels—Determination of Moisture Content—Oven Dry Method—Part 2: Total Moisture—Simplified Method. Beuth Verlag GmbH: Berlin/Heidelberg, Germany, 2010.
25. ICS 75.160.40 (DIN EN ISO 18123); Solid Biofuels—Determination of the Content of Volatile Matter. Beuth Verlag GmbH: Berlin/Heidelberg, Germany, 2016.
26. Dufourny, A.; van de Steene, L.; Humbert, G.; Guibal, D.; Martin, L.; Blin, J. Influence of pyrolysis conditions and the nature of the wood on the quality of charcoal as a reducing agent. *J. Anal. Appl. Pyrolysis* **2019**, *137*, 1–13. [[CrossRef](#)]
27. ICS 19.120 (DIN ISO 9276-2); Representation of Results of Particle Size Analysis—Part 2: Calculation of Average Particle Sizes/Diameters and Moments from Particle Size Distributions. Beuth Verlag GmbH: Berlin/Heidelberg, Germany, 2006.
28. ICS 75.160.40 (DIN EN 15149-1); Solid Biofuels—Determination of Particle Size Distribution—Part 1: Oscillating Screen Method Using Sieve Apertures of 1 Mm and Above. Beuth Verlag GmbH: Berlin/Heidelberg, Germany, 2011.
29. ICS 75.160.40 (DIN EN ISO 18125:2017-08); Solid Biofuels—Determination of Calorific Value. Beuth Verlag GmbH: Berlin/Heidelberg, Germany, 2017.
30. Magnaterra, M.; Fusco, J.R.; Ochoa, J.; Cukierman, A.L. Kinetic Study of the Reaction of Different Hardwood Sawdust Chars with Oxygen. Chemical and Structural Characterization of the Samples. In *Advances in Thermochemical Biomass Conversion*; Bridgwater, A.V., Ed.; Springer: Dordrecht, The Netherlands, 1993; pp. 116–130. ISBN 978-94-010-4582-7.
31. Benson, B.B.; Krause, D. The Concentration and Isotopic Fractionation of Gases Dissolved in Freshwater in Equilibrium with the Atmosphere. 1. Oxygen. Available online: <http://www.jstor.org/stable/2835754> (accessed on 6 August 2021).
32. Jess, A.; Wasserscheid, P. *Chemical Technology: An Integral Textbook*; Wiley-VCH: Weinheim, Germany, 2013; ISBN 978-3-527-30446-2.
33. Baehr, H.D.; Stephan, K. *Wärme- und Stoffübertragung*, 9th ed.; aktualisierte Auflage; Springer Vieweg: Berlin/Heidelberg, Germany, 2016; ISBN 978-3-662-49676-3.
34. Fuller, E.N.; Schettler, P.D.; Giddings, J.C. New method for prediction of binary gas-phase diffusion coefficients. *Ind. Eng. Chem.* **1966**, *58*, 18–27. [[CrossRef](#)]
35. Gradel, A. Gleichstromvergasung von Holzpellets mit integrierter Adsorption von Teerbestandteilen. Ph.D. Thesis, Universität Bayreuth, Bayreuth, Germany, 2020.

36. Kashiwagi, T.; Nambu, H. Global kinetic constants for thermal oxidative degradation of a cellulosic paper. *Combust. Flame* **1992**, *88*, 345–368. [[CrossRef](#)]
37. Várhegyi, G.; Sebestyén, Z.; Czégény, Z.; Lezsovits, F.; Könczöl, S. Combustion Kinetics of Biomass Materials in the Kinetic Regime. *Energy Fuels* **2012**, *26*, 1323–1335. [[CrossRef](#)]
38. Bhatia, S.K.; Perlmutter, D.D. A random pore model for fluid-solid reactions: I. Isothermal, kinetic control. *AIChE J.* **1980**, *26*, 379–386. [[CrossRef](#)]
39. Bhatia, S.K.; Perlmutter, D.D. A random pore model for fluid-solid reactions: II. Diffusion and transport effects. *AIChE J.* **1981**, *27*, 247–254. [[CrossRef](#)]
40. Anca-Couce, A.; Sommersacher, P.; Scharler, R. Online experiments and modelling with a detailed reaction scheme of single particle biomass pyrolysis. *J. Anal. Appl. Pyrolysis* **2017**, *127*, 411–425. [[CrossRef](#)]
41. Grieco, E.; Baldi, G. Analysis and modelling of wood pyrolysis. *Chem. Eng. Sci.* **2011**, *66*, 650–660. [[CrossRef](#)]
42. Di Blasi, C. Combustion and gasification rates of lignocellulosic chars. *Prog. Energy Combust. Sci.* **2009**, *35*, 121–140. [[CrossRef](#)]
43. Schneider, C.; Zeller, M.; Böhm, D.; Kolb, T. Influence of pressure on the gasification kinetics of two high-temperature beech wood chars with CO₂, H₂O and its mixture. *Fuel* **2021**, *299*, 120523. [[CrossRef](#)]
44. Trubetskaya, A. Reactivity Effects of Inorganic Content in Biomass Gasification: A Review. *Energies* **2022**, *15*, 3137. [[CrossRef](#)]
45. Wu, R.; Beutler, J.; Price, C.; Baxter, L.L. Biomass char particle surface area and porosity dynamics during gasification. *Fuel* **2020**, *264*, 116833. [[CrossRef](#)]
46. Liang, D.; Singer, S. Pore-resolving simulations to study the impacts of char morphology on zone II combustion and effectiveness factor models. *Combust. Flame* **2021**, *229*, 111405. [[CrossRef](#)]
47. Nguyen, C.B.; Scherer, J.; Hartwich, M.; Richter, A. The morphology evolution of char particles during conversion processes. *Combust. Flame* **2021**, *226*, 117–128. [[CrossRef](#)]

Disclaimer/Publisher’s Note: The statements, opinions and data contained in all publications are solely those of the individual author(s) and contributor(s) and not of MDPI and/or the editor(s). MDPI and/or the editor(s) disclaim responsibility for any injury to people or property resulting from any ideas, methods, instructions or products referred to in the content.